

## ULTRAVIOLET HALOS AROUND SPIRAL GALAXIES. I. MORPHOLOGY

EDMUND HODGES-KLUCK<sup>1</sup>, JULIAN CAFMEYER<sup>1</sup> & JOEL N. BREGMAN<sup>1</sup>

*accepted by ApJ*

### ABSTRACT

We examine ultraviolet halos around a sample of highly inclined galaxies within 25 Mpc to measure their morphology and luminosity. Despite contamination from galactic light scattered into the wings of the point-spread function, we find that UV halos occur around each galaxy in our sample. Around most galaxies the halos form a thick, diffuse disk-like structure, but starburst galaxies with galactic superwinds have qualitatively different halos that are more extensive and have filamentary structure. The spatial coincidence of the UV halos above star-forming regions, the lack of consistent association with outflows or extraplanar ionized gas, and the strong correlation between the halo and galaxy UV luminosity suggest that the UV light is an extragalactic reflection nebula. UV halos may thus represent  $10^6 - 10^7 M_{\odot}$  of dust within 2–10 kpc of the disk, whose properties may change with height in starburst galaxies.

*Subject headings:* galaxies: halos — ISM: dust, extinction — ultraviolet: galaxies

### 1. INTRODUCTION

Dust plays an important role in galaxies as a catalyst for instellar chemistry, a repository of metals, and a heat source for interstellar gas. The discovery that there is about as much dust outside of galaxies as within (Ménard et al. 2010) suggests that dust also plays an important role in the disk-halo cycle (however, see Smith et al. 2016, who argue for a smaller amount of halo dust). Dust is primarily formed in the atmospheres of evolved stars or supernova remnants, so extragalactic dust was likely transported out of the disk by gaseous flows (e.g., Ferrara et al. 1991). Indeed, dusty outflows have been detected around edge-on galaxies, including filaments seen in extinction (Howk & Savage 1997, 1999) and dust emission at several kpc above the midplane (McCormick et al. 2013; Meléndez et al. 2015). Still, it remains unclear how and when the dust gets into the halo, how long it remains there, and whether it is altered in the process. These issues motivate further studies.

Extragalactic dust can be studied through extinction, emission, or reflection (scattering). In the first case, extraplanar dust lanes can be seen against the thick disk of stellar light (Howk & Savage 1997), but above a few kpc from the galaxy midplane the extinction must be measured toward background continuum sources, such as quasars. Since there are few quasars behind any one galaxy, Ménard et al. (2010) stacked many sources to measure the extinction to beyond 1 Mpc. In contrast, thermal emission or reflection will only be seen near the galaxy, since both processes need a nearby light source. This makes edge-on systems the ideal laboratories to isolate extraplanar dust emission and scattered light.

The possibility of extragalactic reflection nebulae (eRN) around edge-on galaxies was raised by Ferrara et al. (1996), and Hoopes et al. (2005) reported the discovery of diffuse ultraviolet (UV) light consistent with an eRN above the disks of the edge-on starburst galaxies M82 and NGC 253. This conclusion was re-

inforced by Hutton et al. (2014), and Seon et al. (2014) detected a UV halo around NGC 891 that they argue is also an eRN. In Hodges-Kluck & Bregman (2014, hereafter, HKB14) we reported that UV halos are ubiquitous around highly inclined galaxies, but Sandin (2015) pointed out that the light scattered into the wings of the point-spread function (PSF) can masquerade as a physical halo. Shinn & Seon (2015) modeled several of the galaxies in HKB14 including this effect, and found that some of the UV halos we had reported are astrophysical while others are artificial. In principle, eRN are visible at other wavelengths, and some of the H $\alpha$  attributed to extraplanar diffuse ionized gas (eDIG) may actually be reflected light (Ferrara et al. 1996; Seon et al. 2014). However, UV halos are especially promising because the scattering cross-section is high in the UV for typical dust compositions and the sky is relatively dark.

In HKB14 we examined galaxies with both *Swift* UVOT (Roming et al. 2005) and *GALEX* (Martin et al. 2005) observations, regardless of physical properties. In a series of three papers we now take a more systematic approach to measuring the physical properties of the UV halos around highly inclined spiral galaxies. In this paper (Paper I) we focus on galaxies within about 25 Mpc to determine the frequency of physical UV halos, their morphology, and whether they are eRN. The subsequent papers will present a catalog of total halo fluxes for a wider sample where morphology cannot necessarily be measured (Paper II), and models of the spectral energy distributions (SEDs) for those galaxies with the highest quality data (Paper III).

The remainder of this paper is organized as follows: Section 2 describes our sample and data sources, and Section 3 is focused on correcting for galactic light scattered into the PSF wings. In Section 4 we describe the morphology of the UV halos and compare them to diffuse halos at other wavelengths, and in Section 5 we use information from the halo fluxes in each filter to characterize the UV halos. We interpret the results in Section 6 to argue that the UV halos are likely eRN and connect the UV measurements to extinction and emission mea-

hodgekl@umich.edu

<sup>1</sup> Department of Astronomy, University of Michigan, Ann Arbor, MI 48109

TABLE 1  
 BASIC GALAXY PARAMETERS

Name	Type	$T$	$i$	$M_B$	$d$	$v_{\text{rot}}$	$E(B-V)$	$B-V$	$m_K$	$M_*$	$L_{\text{H}\alpha}$	SFR(IR)
(1)	(2)	(3)	(deg)	(mag)	(Mpc)	( $\text{km s}^{-1}$ )	(mag)	(mag)	(mag)	( $10^{10} M_{\odot}$ )	( $10^{40} \text{ erg s}^{-1}$ )	( $M_{\odot} \text{ yr}^{-1}$ )
Starbursts												
NGC0253	SABc	5.1	90	-21.23	3.25	189.8	0.019	0.69	3.772	4.36	9.59	3.97
M82	Scd	7.5	76.9	-20.13	3.93	65.6	0.138	0.68	4.665	1.83	15.0	9.42
NGC4631	SBcd	6.6	90	-22.42	6.02	138.4	0.015	0.39	6.465	0.98	15.0	1.03
NGC3628	Sb	3.1	79.3	-21.54	10.89	215.4	0.024	0.68	6.074	4.47	4.59	3.30
NGC4666	SABc	5.1	69.6	-21.10	17.28	192.9	0.022	0.64	7.055	3.10	16.8	4.83
NGC3079	SBcd	6.6	90	-21.56	19.28	208.4	0.01	0.53	7.262	2.91	16.9	8.17
NGC5775	SBc	5.2	83.2	-21.09	20.34	187.2	0.037	0.66	7.763	2.45	0.014	3.97
NGC4388	Sb	2.7	90	-22.13	20.5	171.2	0.029	0.57	8.004	1.55	2.35	3.16
Normal Spirals												
NGC0055	SBm	8.8	90	-20.09	1.94	58.7	0.012	0.33	6.249	0.09	3.42	0.06
NGC0891	Sb	3.1	90	-20.37	9.96	212.1	0.058	0.70	5.938	3.99	5.30	2.43
NGC2683	Sb	3.0	82.8	-20.42	10.08	202.6	0.029	0.75	6.328	2.98	5.56	0.41
NGC4517	Sc	6.0	90	-21.46	10.56	139.6	0.021	0.53	7.329	0.73	5.56	0.34
NGC4565	Sb	3.3	90	-22.55	12.18	243.6	0.014	0.68	6.060	5.65	2.20	0.80
NGC4096	SABc	5.3	80.5	-20.39	12.68	144.8	0.016	0.50	7.806	0.088	5.18	0.56
NGC4313	Sab	2.1	90	-20.16	14.62	117.6	0.033		8.468			0.37
NGC3623	Sa	1.0	90	-21.02	12.77	231.2	0.022	0.78	6.066	7.17	5.76	0.38
NGC5907	SABc	5.3	90	-21.08	16.37	226.6	0.009	0.62	6.757	5.03	14.1	2.04
NGC4216	SABb	3.0	90	-20.80	16.78	244	0.028	0.83	6.524	6.06		0.44
NGC4607	SBbc	4.0	90	-20.18	17.78	98.9	0.028	0.75	9.584	0.60	1.17	0.68
NGC4522	SBc	5.9	79.2	-20.91	18.29	96.4	0.018		9.8		1.67	0.40
NGC0134	SABb	4.0	90	-21.49	18.71	220.2	0.016	0.69	6.844	5.95		4.51
NGC4157	SABb	3.3	90	-19.88	18.7	188.9	0.019	0.64	7.363	3.03	8.11	2.71
ESO358-063	Scd	6.9	75.6	-20.34	18.98	135	0.005	0.7	9.144	0.61		0.87
NGC4217	Sb	3.1	81	-20.08	19.37	187.6	0.015	0.75	7.582	3.67	3.08	
NGC4330	Sc	6.0	78.9	-20.02	19.61	115.7	0.021		9.51			0.36
NGC3044	SBc	5.5	90	-20.32	22.48	152.6	0.022	0.6	8.982	1.01	15.1	2.77
NGC5170	Sc	4.9	90	-21.13	26.8	244.7	0.07	0.7	7.628	7.46		0.79

REFERENCES. — Values from the NASA/IPAC Extragalactic Database, (<http://ned.ipac.caltech.edu/>), HyperLeda Makarov et al. (2014) and the IRAS catalog (<http://irsa.ipac.caltech.edu/Missions/iras.html>).

NOTE. — Cols. (1) Name (2) Morphological Type (3) Morphological type code (4) Inclination angle (5)  $B$  magnitude (6) Distance (7) Circular rotational velocity (8) Foreground Galactic extinction (9)  $B-V$  color (10)  $K$ -band magnitude from the 2MASS Extended Source Catalog Schlafly & Finkbeiner (2011) (11) Stellar mass using relation from Bell & de Jong (2001) (12)  $\text{H}\alpha$  Luminosity (13) Star-formation rate estimated from the Kennicutt (1998) relation  $\text{SFR} = 4.5 \times 10^{-44} L_{\text{IR}} M_{\odot} \text{ yr}^{-1}$ .  $L_{\text{IR}}$  we measure as defined by Rice et al. (1988)  $L_{\text{IR}} = 5.67 \times 10^5 d_{\text{Mpc}}^2 (13.48 f_{12} + 5.16 f_{25} + 2.58 f_{60} + f_{100}) L_{\odot}$ , where the fluxes at 12, 25, 60, and 100  $\mu\text{m}$  are in Jy from the IRAS catalog.

surements. Section 7 summarizes the paper and presents our main conclusions.

## 2. DATA

Our goal is to measure the structure of the diffuse extraplanar UV light, so we limit the sample to nearby, highly inclined, spiral galaxies. The initial sample (drawn from the HyperLeda database<sup>2</sup>; Makarov et al. 2014) includes galaxies within 25 Mpc with an inclination angle of  $i \geq 80^\circ$ , a Hubble type of Sa or later, and an absolute  $B$ -band magnitude of  $M_B < -20$  mag. The distance limit is based on the need for high  $S/N$  in small regions. We excluded some galaxies for which the inclination angles or types were obviously incorrect, and for our distance cut we used the redshift-independent distances from NASA/IPAC Extragalactic Database<sup>3</sup> instead of the HyperLeda values. The initial sample includes 78 galaxies.

Each galaxy must have moderately deep data in at least one of the *GALEX* or *Swift* UVOT filters: *GALEX* FUV ( $\lambda 1516\text{\AA}$ ) and NUV ( $\lambda 2267\text{\AA}$ ), or the UVOT *uvw1*

( $\lambda 2600\text{\AA}$ ), *uvm2* ( $\lambda 2246\text{\AA}$ ), and *uvw2* ( $\lambda 1928\text{\AA}$ ) filters. Most of the data come from the *GALEX* or *Swift* archives, but we also obtained new UVOT data for several targets through the *Swift* program GO 1013198. Based on our prior work, we expect a UV halo flux that is about 1% of the total galaxy flux, so to accumulate enough  $S/N$  we require exposure times greater than 2-4 ks in either *GALEX* filter or 5-6 ks in any UVOT filter (this excludes the 600s exposures from the *GALEX* all-sky imaging survey). We excluded galaxies that are in regions with strongly variable Galactic cirrus or are in very crowded fields. *Swift* targets must also fit within the  $17 \times 17$  arcmin field of view for accurate background subtraction. The 26 galaxies that meet this criteria form our working sample, and the basic properties of these objects are given in Table 1. The UV exposure times and  $3\sigma$  point-source sensitivities are given in Table 2. The observation IDs used in this paper are given in the Appendix.

Our reliance on archival data means that the sensitivity and filter coverage vary widely among the galaxies. We also note that a disproportionate number of galaxies are in the Virgo Cluster, which has been observed extensively. Some of the galaxies are included in published

<sup>2</sup> <http://leda.univ-lyon1.fr/>

<sup>3</sup> <http://ned.ipac.caltech.edu/>

TABLE 2  
OBSERVATIONS

Name	Exposure Time (s)					Sensitivity (AB mag)					H $\alpha$	Radio	21cm
(1)	FUV (2)	NUV (3)	<i>uvw2</i> (4)	<i>uvm2</i> (5)	<i>uvw1</i> (6)	FUV (7)	NUV (8)	<i>uvw2</i> (9)	<i>uvm2</i> (10)	<i>uvw1</i> (11)	(12)	(13)	(14)
Starbursts													
NGC0253	3281	15043				25.0	26.1					5	13
M82	14707	29422	91603	147713	92788	25.9	26.4	26.8	25.7	26.5	10	21	24
NGC4631	3147	3147	1377	5474	1123	24.9	25.1	24.0	24.7	23.6	10	21	19
NGC3628	5812	17076	8095	5530	3546	25.4	26.0	25.2	24.8	24.3		21	6
NGC4666	5940	5940	19561	19610	9858	25.4	25.3	24.7	25.7	25.1		21	18
NGC3079	16108	16108	8512	7252	273	26.3	26.1	25.4	25.1	22.5	23	21	7
NGC5775	2587	5770	14978	23677	4180	24.6	25.4	25.6	25.8	24.5	4	21	8
NGC4388	2538	4993	10331	7334	5331	24.6	25.3	25.4	25.0	24.7	16	21	3
Normal Spirals													
NGC0055	29347	30691				25.5	26.5						20
NGC0891	6047	6283	15353	15200	9787	25.0	25.2	25.7	25.5	25.2	16	21	14
NGC2683	1600	1600	6407	5644	4824	24.3	24.5	25.0	24.8	25.3	16	21	17
NGC4517	1906	6403				23.8	25.5						
NGC4565	12050						25.9					21	25
NGC4096	1650	1650	2670	3575		24.3	24.7	24.6	24.5		10		
NGC4313	3862	3862				24.2	25.2						
NGC3623	1656	1656	5300	7122	3193	24.3	24.6	25.2	25.1	24.5	10	5	6
NGC5907	1543	5423	31888	45601	26482	24.2	25.5	26.3	26.3	26.0	15	21	1
NGC4216	1672	2604				24.3	24.9				16	5	3
NGC4607	2701	6181				24.7	25.5				11		3
NGC4522	2496	2496				24.7	24.9				11		9
NGC0134	5998	6336	4032			25.1	24.9	24.6					
NGC4157	2494	1288				24.7	24.5				23	21	22
ESO358	2456	3197				24.7	25.2						
NGC4217	11774	11774				25.8	25.9				15	21	1
NGC4330	3862	3862	2429	2429	2279	25.1	25.2	24.3	24.1	24.0			3
NGC3044	1676	1676	2910	2910	2585	24.3	24.6				4	21	12
NGC5170	1606	3307				24.0	24.9						2

REFERENCES. — H $\alpha$  and radio references: (1) Allaert et al. (2015) (2) Bottema et al. (1987) (3) Chung et al. (2009) (4) Collins et al. (2000) (5) Condon (1987) (6) Haynes et al. (1979) (7) Irwin et al. (1987) (8) Irwin (1994) (9) Kenney & Koopmann (2001) (10) Kennicutt et al. (2008) (11) Koopmann et al. (2001) (12) Lee & Irwin (1997) (13) Lucero et al. (2015) (14) Oosterloo et al. (2007) (15) Rand (1996) (16) Rossa & Dettmar (2003a) (17) Vollmer et al. (2016) (18) Walter et al. (2004) (19) Wellichew et al. (1978) (20) Westmeier et al. (2013) (21) Wiegert et al. (2015) (22) Yim et al. (2014) (23) Young et al. (1996) (24) Yun et al. (1994) (25) Zschaechner et al. (2012)

NOTE. — Cols. (2-6) Exposure times (7-11)  $3\sigma$  point-source sensitivity (12-14) References for non-UV data used here.

work on UV halos (Hoopes et al. 2005; Hutton et al. 2014; Seon et al. 2014; Hodges-Kluck & Bregman 2014; Shinn & Seon 2015; Baes & Viaene 2016).

We processed the data for each galaxy as described in HKB14, including cleaning the UVOT and *GALEX* images of diffuse artifacts in each exposure. We combined the *Swift* exposures for each filter into a single, exposure-corrected image. We masked all the point sources outside the galaxy that were detected at  $3\sigma$  or greater, and we also masked each source detected at  $4\sigma$  or greater in any one filter in all the remaining filters. This helps to exclude stars that are close to the galaxy but are not formally detected at different wavelengths or in shorter observations.

### 3. EXTENDED PSF WINGS AND HALO LIGHT

Sandin (2015) showed that the diffuse light around edge-on galaxies consists in part of light from the galaxy image scattered into the wings of the PSF (the Airy pattern), since the sum of many overlapping Airy patterns leads to a diffuse glow around the galaxy. To measure and subtract this component, a PSF must be measured to at least twice the angular size of the galaxy. Hereafter, we refer to this light as “PSF-wing contamination.” Shinn & Seon (2015) were the first to address this issue

in the *GALEX* FUV filter, and here we extend their analysis by measuring and extrapolating the PSFs for each filter in order to determine the PSF-wing contamination in the measured halo fluxes. We want to obtain accurate 2D maps of the halo rather than only a profile along the minor axis, so the typical approach of convolving a model with the PSF is not sufficient.

#### 3.1. Measured PSFs

The *GALEX* and *Swift* calibration teams have provided PSFs measured to radii of about 60 and 30 arcsec, respectively<sup>4</sup>, but for the galaxies in this work the PSFs need to extend to 200-600arcsec. Extrapolating the wings from the available PSFs may not be sufficient, so we measured PSFs from bright point sources to better characterize the wings.

For *GALEX*, we used deep observations of the quasars 3C 273 (30 ks, tile GI4\_012003\_3C273) and PKS 2155 – 304 (32 ks, tile PKS2155m304), which are relatively isolated on the sky and not bright enough to produce strong ghost images or diffraction spikes. These quasars are too bright to measure extended PSFs with *Swift*, so we used

<sup>4</sup> see <http://www.galex.caltech.edu/researcher/techdoc-ch5.html> and <http://heasarc.gsfc.nasa.gov/docs/heasarc/caldb/swift/docs/uvot/>

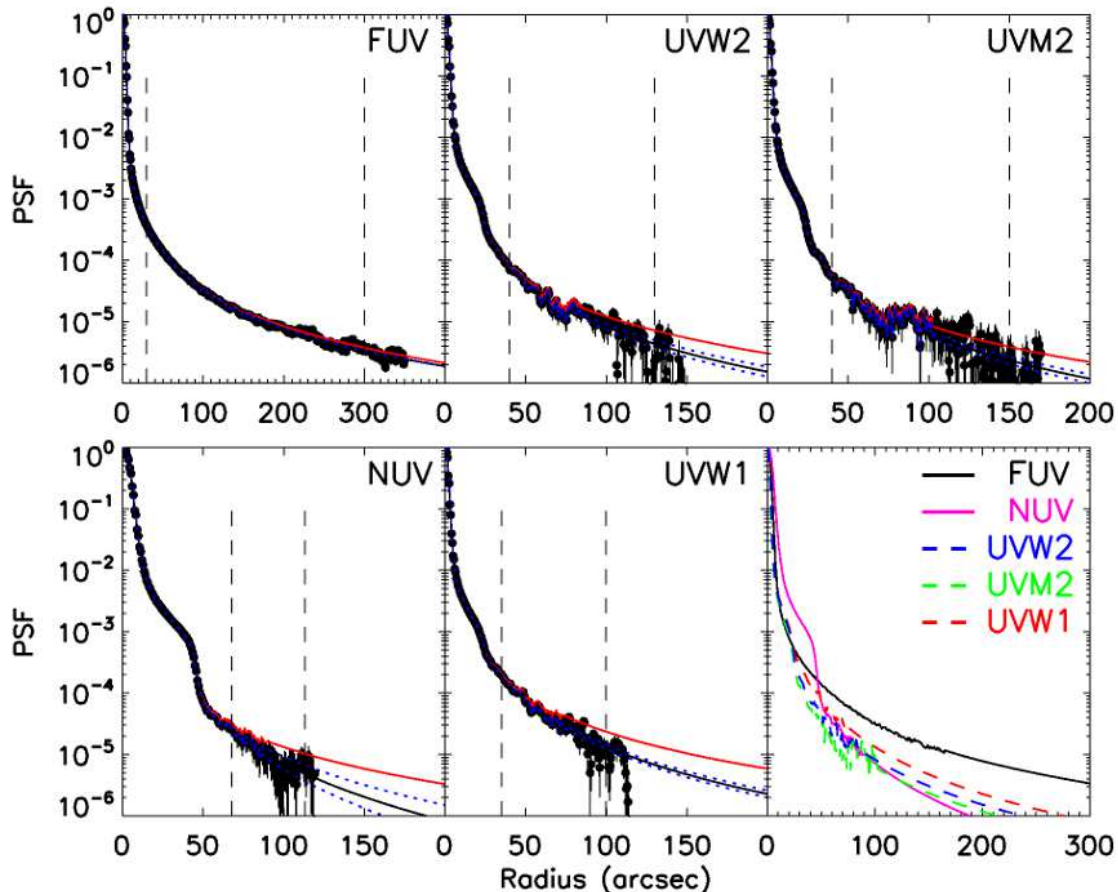


FIG. 1.— Measured, radially-averaged PSF profiles for each filter (filled circles) and the best-fit profile (black solid line). The fit is based on points between the vertical dashed lines, and the profile is extrapolated from the data starting halfway between these lines. The statistical  $1\sigma$  error bars on the fit are shown as dashed lines. For comparison, the  $r^{-2}$  profile is shown as a red line. The last panel shows the extrapolated profiles to a radius of 300 arcsec for each filter.

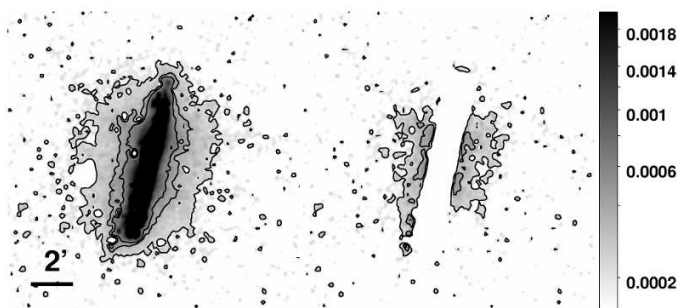


FIG. 2.— *Left*: The FUV image of NGC 3079 before correcting for galactic light scattered into the PSF wings. The contours are 3, 4, and  $5\sigma$  above background. *Right*: The same image after correction for PSF-wing contamination. The galaxy image used to compute the correction has been masked.

a combined image of Mrk 501, which has an effective exposure of 129 ks in *uvw1*, 131 ks in *uvm2*, and 170 ks in *uvw2*. The data were processed as described above and in HKB14, except that we used at least fifteen sources to compute the astrometric solution for each image and we rejected images where the source was outside a few arcminutes from the chip center. The observation IDs we used are given in the Appendix.

We then measured the PSF by constructing an az-

imuthally symmetric radial profile to  $r > 100$  arcsec. The actual PSF is not azimuthally symmetric, but simulations show that unless it is very asymmetric (to an extent that would be noticeable on the image), this approximation does not noticeably change the measured PSF-wing contamination for any galaxy with a projected size of about an arcminute or more (even at smaller sizes, it will not usually make a difference). The background level is crucial to measuring the small amount of light scattered by the PSF to large radii, so we masked all point sources detected using the *Swift* task *uvotdetect* with a  $3\sigma$  detection threshold (based on SExtractor; Bertin & Arnouts 1996) other than the target. Since these sources are *much* fainter than the target, we assume that masking to the nominal 99% encircled energy radius is sufficient.

The measured profiles are shown in Figure 1, along with fitted profiles of the form  $Ar^{-x} + B$ , where  $A$ ,  $B$ , and  $x$  are determined using least-squares fits to the data between the dashed vertical lines in Figure 1 (in each plot,  $B$  has been subtracted). For comparison, we also plot a fitted profile where  $x \equiv 2$ . The extrapolation based on the best-fit model begins at the midpoint between the dashed vertical lines, but our results are insensitive to where we match the extrapolated profile to the measured one. The FUV is close to  $x = 2$  at all radii, but the other

TABLE 3  
PSF WING EXPONENTS

Filter	Exponent	Filter	Exponent
FUV	$2.05 \pm 0.01$	<i>wvm2</i>	$2.4 \pm 0.1$
NUV	$3.1 \pm 0.3$	<i>www1</i>	$2.55 \pm 0.08$
<i>www2</i>	$2.4 \pm 0.1$		

NOTE. — Best-fit exponents ( $x$  in  $r^{-x}$ ) and statistical errors from the PSF profile fitting.

filters concentrate light within about 30 arcsec, with the subsequent decay being steeper than  $x = 2$ .

The best-fit exponents are given in Table 3. The fit depends strongly on  $B$ , so we verified that the background level in the fitting zone was consistent with the background measured outside the fitting zone. We also repeated the analysis using a  $2\sigma$  threshold for point source removal and measured  $x$  values that are consistent with the earlier measurements. Finally, we verified that the PSFs successfully clean the outer regions in the source images and other images of bright point sources (within  $\sim 10$  arcsec an azimuthally symmetric PSF is a poor match to the data).

There are two caveats to this analysis. First, the PSF becomes increasingly distorted with increasing distance from the optical axis, so for images “far” from the optical axis the assumption of radial symmetry is badly wrong (where the critical distance depends on the instrument). The PSF is naturally hard to measure to large radii far from the optical axis, and there are few bright sources that are both near the chip edge and have very deep *GALEX* or *Swift* data. Thus, for galaxies near the chip edge the measured PSFs may not accurately account for the PSF-wing contamination.

Second, the PSF may vary with time (Sandin 2015, although the variability is probably much larger for ground-based instruments). We could not make useful tests with *GALEX* data because the bright sources we used for comparison typically had different PSF cores that were obviously due to the different positions on the chip. For *Swift* we selected all exposures of Mrk 501 in a given filter where the source was within 1 arcmin of the chip center, and searched for variability in the best-fit  $x$  between combined images taken in different months. We found no clear variability, but some low level of variability beyond 50 arcsec is possible. We note that the *Swift* PSF *core* does vary with time in the sense that the full-width at half maximum depends on the temperature of the UVOT focusing rods<sup>5</sup>. However, we did not find any variation in the best-fit exponent for the PSF wings.

Our results are consistent with the best-fit exponents found in other sources where the PSF cannot be measured to such large distances, so we believe that the fits are reasonably accurate.

### 3.2. Estimating the PSF-wing Contamination

We estimated the PSF-wing contamination for each image by creating a model using the input image and the extrapolated PSF models, using the best-fit exponent for each filter (Table 3). We first clipped the input image to the region that just contains the galaxy. We did not

use an objectively defined region because of the varied disk morphologies and inclinations in our sample, but the galaxy regions are conservative in that they extend to at least 2 kpc above the midplane. We then convolved the clipped image with a PSF model that was extrapolated to at least twice the angular diameter of the galaxy.

The resulting image shows the amplitude of the PSF-wing light at each position around the galaxy, but the total flux in the model image is too low and the light is too smeared out because we do not deconvolve the galaxy image before convolving it with the extrapolated PSF (the galaxy is too complex for accurate deconvolution). The former effect is corrected by multiplying the fake image by the ratio of the flux in the galaxy in the original and fake images (this is not an exact correction, but simulations of exponential disk models show that it underestimates the PSF-wing flux by much less than the statistical uncertainties for our sample). The latter effect cannot be easily corrected, but we find (again using simulations of exponential disk models) that the most severe impact is within about 10 pixels of bright regions in each galaxy, and in practice the galaxy regions we define extend at least this far from bright clumps. The combination of these issues leads to an overestimate of the PSF-wing contamination by about 10% immediately adjacent to the galaxy, and which quickly declines with height. We also investigated the error due to using a symmetric PSF in the FUV, where the PSF is measured to over 100 arcsec. We convolved model images with angular sizes smaller than this with our model PSFs and the measured PSF. This leads to differences of 0-3% in the PSF-wing light measured around the galaxy. On the scale of the whole halo, these effects are very modest.

The model image can then be used in conjunction with the original image to measure the PSF-wing contamination at any point in the halo, and we also subtract the model from the original to create corrected halo images. The PSF-wing contamination differs for each galaxy and filter, but it ranges from 1-90% of the total extraplanar flux in our sample. The contamination is generally larger in the FUV than the other filters. The importance of the correction is illustrated in Figure 2 for NGC 3079, where we show FUV images before and after subtracting the model image. We verified the Sandin (2015) proposition that convolving the galaxy image with a PSF extrapolated to more than twice the angular size of the galaxy does not significantly alter the PSF-wing contamination. In Section 5 we assess the reliability of our PSF-wing subtraction.

## 4. EXTRAPLANAR ULTRAVIOLET MORPHOLOGY

In this section we describe the qualitative structure of the diffuse extraplanar UV light in our sample and compare it to the diffuse structure seen at other wavelengths where the source of the light is basically understood. The initial work on UV halos (Hoopes et al. 2005) focused on galaxies with galactic superwinds, and in this section we divide our sample into galaxies with known winds (starburst galaxies) and those without (normal galaxies).

### 4.1. Existence of UV Halos

We use UV images where the PSF-wing contamination has been subtracted. Figures 3 and 4 show the images

<sup>5</sup> <https://heasarc.gsfc.nasa.gov/ftools/caldb/help/uvotapercorr.html>

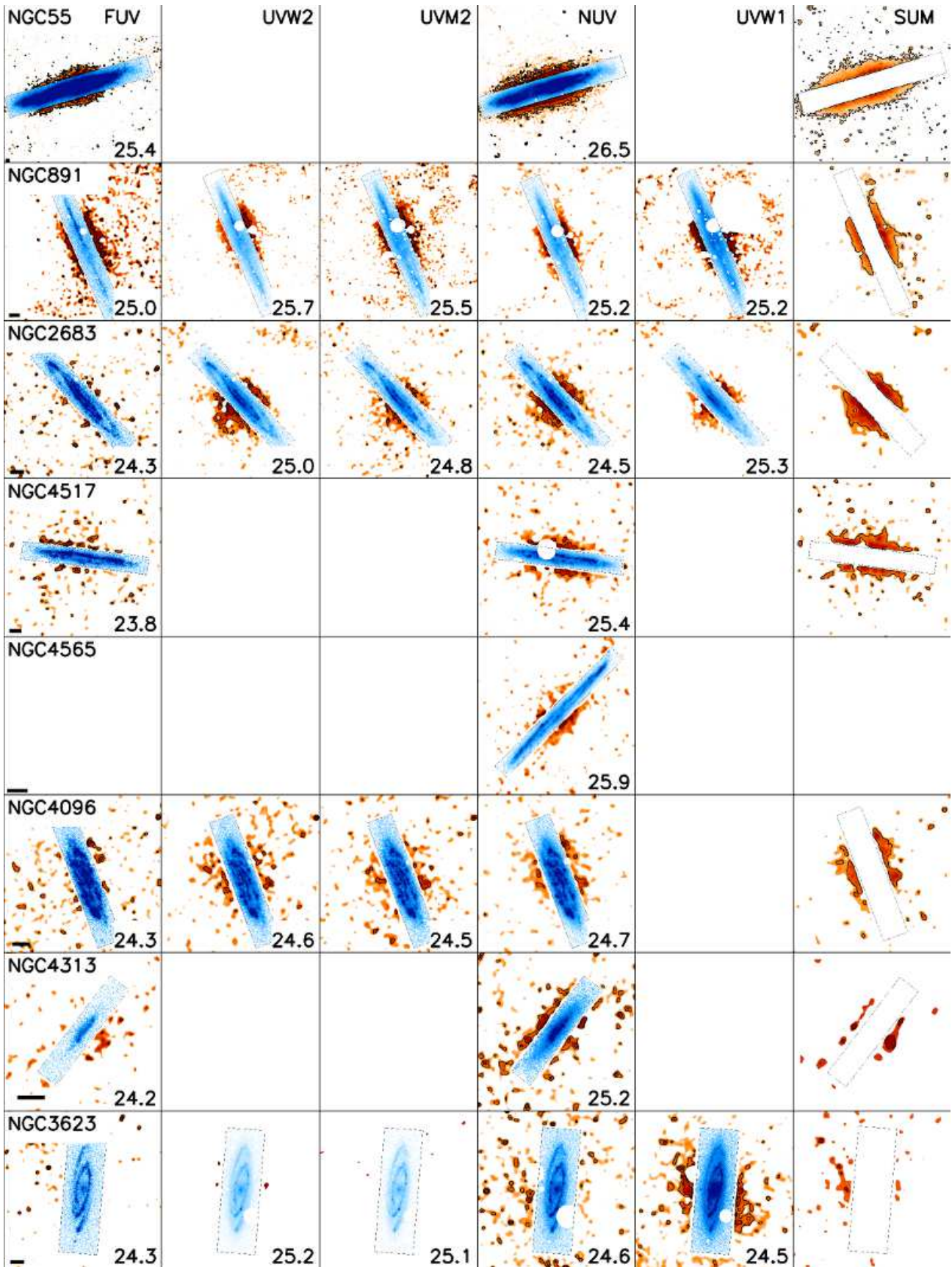


FIG. 3.— UV halos (orange) around normal galaxies in the *GALEX* and UVOT filters, shown with increasing wavelength from left to right. The final column shows the combined data, referenced to the *GALEX* resolution. The orange maps have been corrected for the PSF-wing contamination from the galaxy (image shown in blue) and point sources have been masked. For each filter, the contours are the 2, 4, 8, and  $16\sigma$  contours above the background. A 2 arcmin line is shown at the bottom left of each row, and the  $3\sigma$  point-source sensitivity for the map is shown at the bottom right of each panel. The composite image only shows the  $3\sigma$  contour.

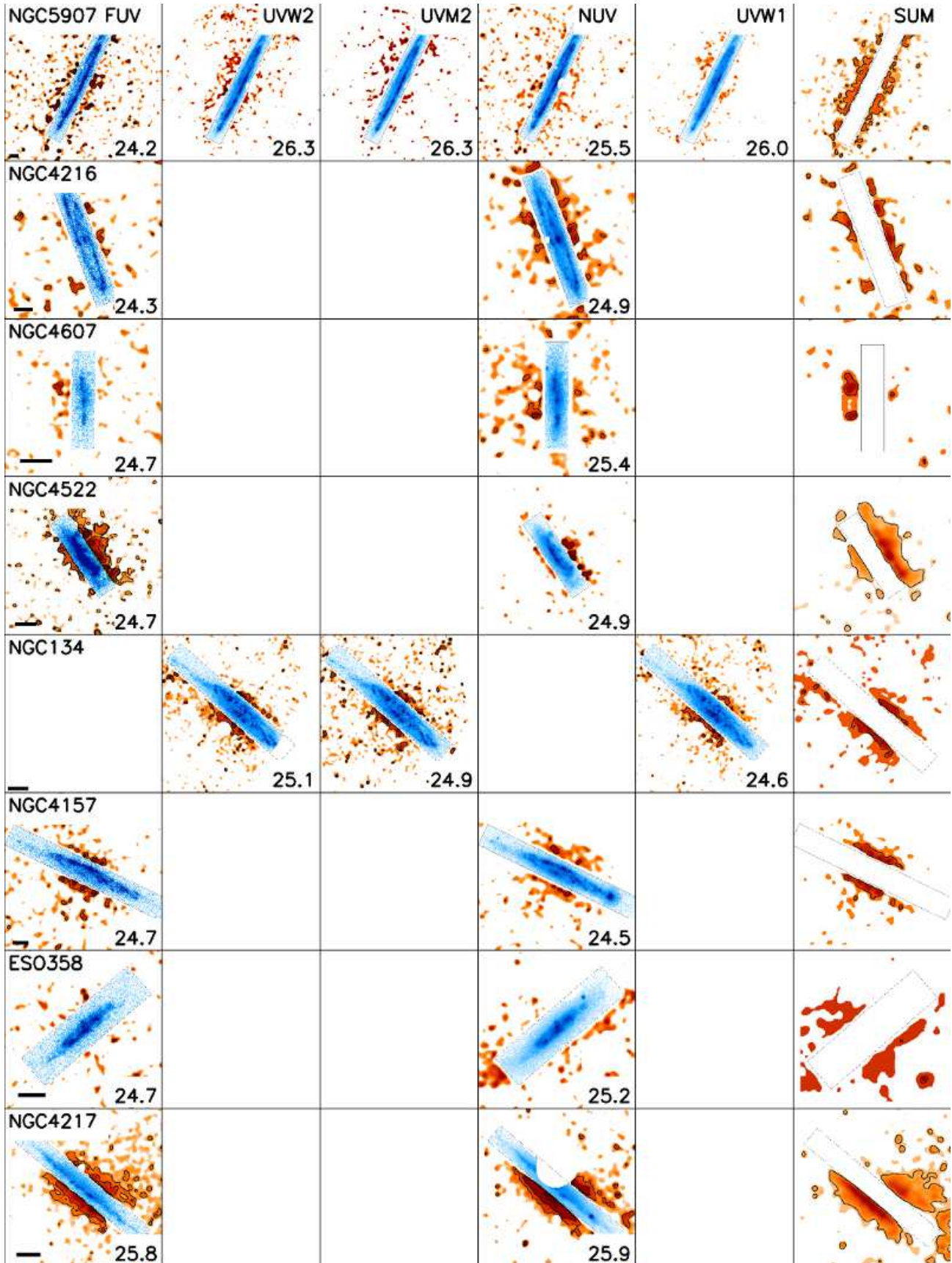


FIG. 3.— continued

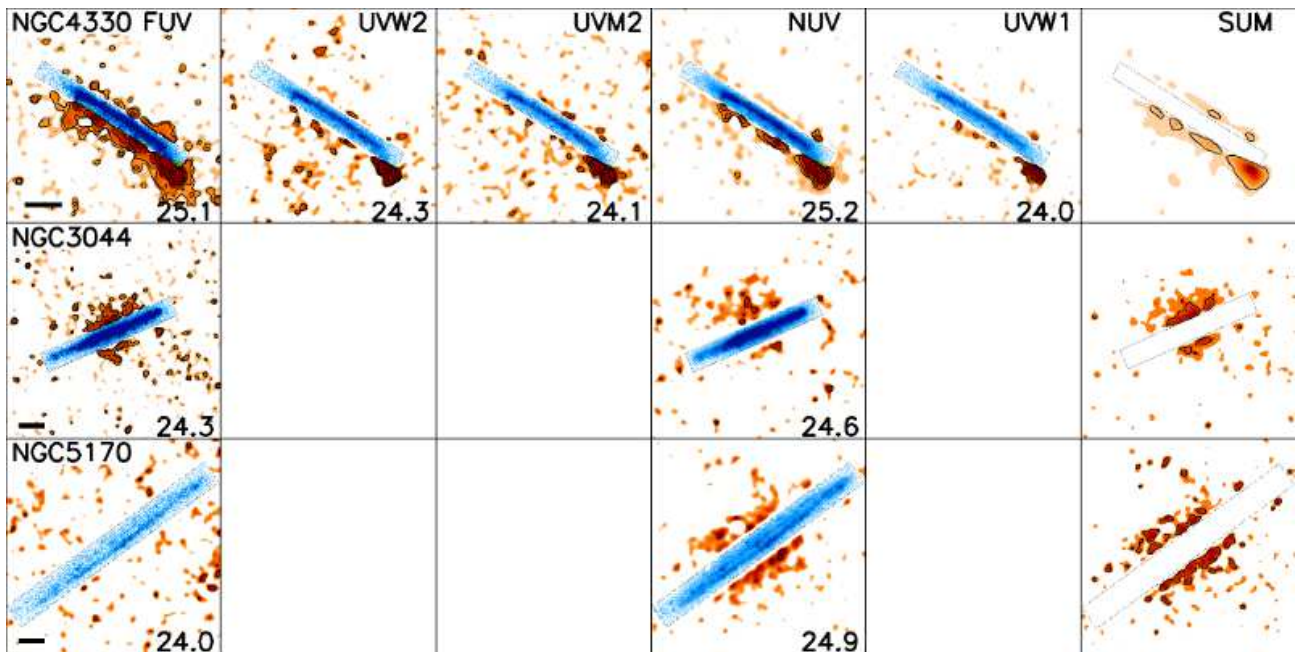


FIG. 3.— continued

in each filter for the normal and starburst galaxies, respectively. In these images, the galaxy region used to estimate the PSF-wing contamination is masked, so we superimpose the unsmoothed image of the galaxy for that filter in this region (in blue). Outside of this region, point sources have been masked, the image has been smoothed with a Gaussian kernel (with  $\sigma = 3 - 8$  pixels, depending on the angular size of the galaxy), and the image has been clipped to  $1\sigma$  above the background. The contours show the  $2$ ,  $4$ ,  $8$ , and  $16\sigma$  level above the background. For each image we also list the  $3\sigma$  point-source sensitivity in AB magnitudes (Oke & Gunn 1983), which shows the differences in depth between filters.

Although the UVOT and *GALEX* images have different PSFs, artifacts, and systematic uncertainties, the morphology of the residual extraplanar UV light is similar between filters for most galaxies, so UV halos appear to be physical phenomena. Thus, in the final columns of Figures 3 and 4 we show a composite image for each galaxy made by summing each filter (referenced to the effective area of the *uvm2* filter). These images have roughly twice the  $S/N$  of the images in each filter, so they highlight the extent of the halo. Remarkably, every galaxy in the sample has a UV halo extending at least to 6 kpc above the midplane. Considering that our selection criteria were distance, luminosity, and inclination, this suggests that UV halos are a common feature of luminous spiral galaxies.

There are some differences between filters for several galaxies that may be artificial. For example, in the *uvw2* images of NGC 4666 and NGC 5775 (Figure 4), the halo appears to be more prominent than in the *uvm2* or FUV images, even though the *uvm2* has a higher sensitivity. This may indicate residual light in the central 2 arcmin halo ring in the large-scale *uvw2* scattered-light artifact (HKB14), which could mimic a halo in an image centered on the galaxy. The smaller field of view of the UVOT can also lead to differences: in the relatively shallow UVOT

images of NGC 4631 (Figure 4), the halo is both less prominent and more symmetric than in the *GALEX* images. This probably results from the “background” regions in the UVOT being inside the UV halo itself, a scenario that is supported by the *GALEX* images. In other cases, differences between the morphology in each filter likely indicate physical differences. For example, in M82 and NGC 253 (Figure 4), the NUV halo appears more like a thick disk than the FUV halo, which is more filamentary in nature. This morphology cannot be explained by PSF-wing contamination or filter artifacts.

We investigated the contribution of stellar clusters or background sources to the diffuse light in those galaxies with *HST* observations in the *U* band or bluer. For these objects, we identified point-like sources in the *HST* maps that were not already identified and removed in our maps and predicted a *Swift* or *GALEX* flux for each, assuming that each source has the spectrum of a B star. We then compared the flux to the total diffuse UV flux, and found that it can explain at most a few percent of the light. The exception that proves the rule is NGC 4522, where the Virgo cluster is stripping the ISM (Kenney & Koopmann 1999) and there are known stellar clusters in the halo. In this case, most of the flux in the FUV comes from these clusters. Even NGC 4522 has a diffuse component, however, so we conclude that all of these galaxies have true diffuse UV halos.

#### 4.2. Ultraviolet Morphology

There are three qualitative morphological metrics we use to compare the UV halos in our sample: filamentary structure, concentration of the UV light (both in the vertical direction and along the disk), and symmetry across the midplane. In general, these are consistent among filters for a given galaxy.

*Filaments*— Filaments are most easily visible in the FUV, and they are seen in most starburst galaxies (M82,



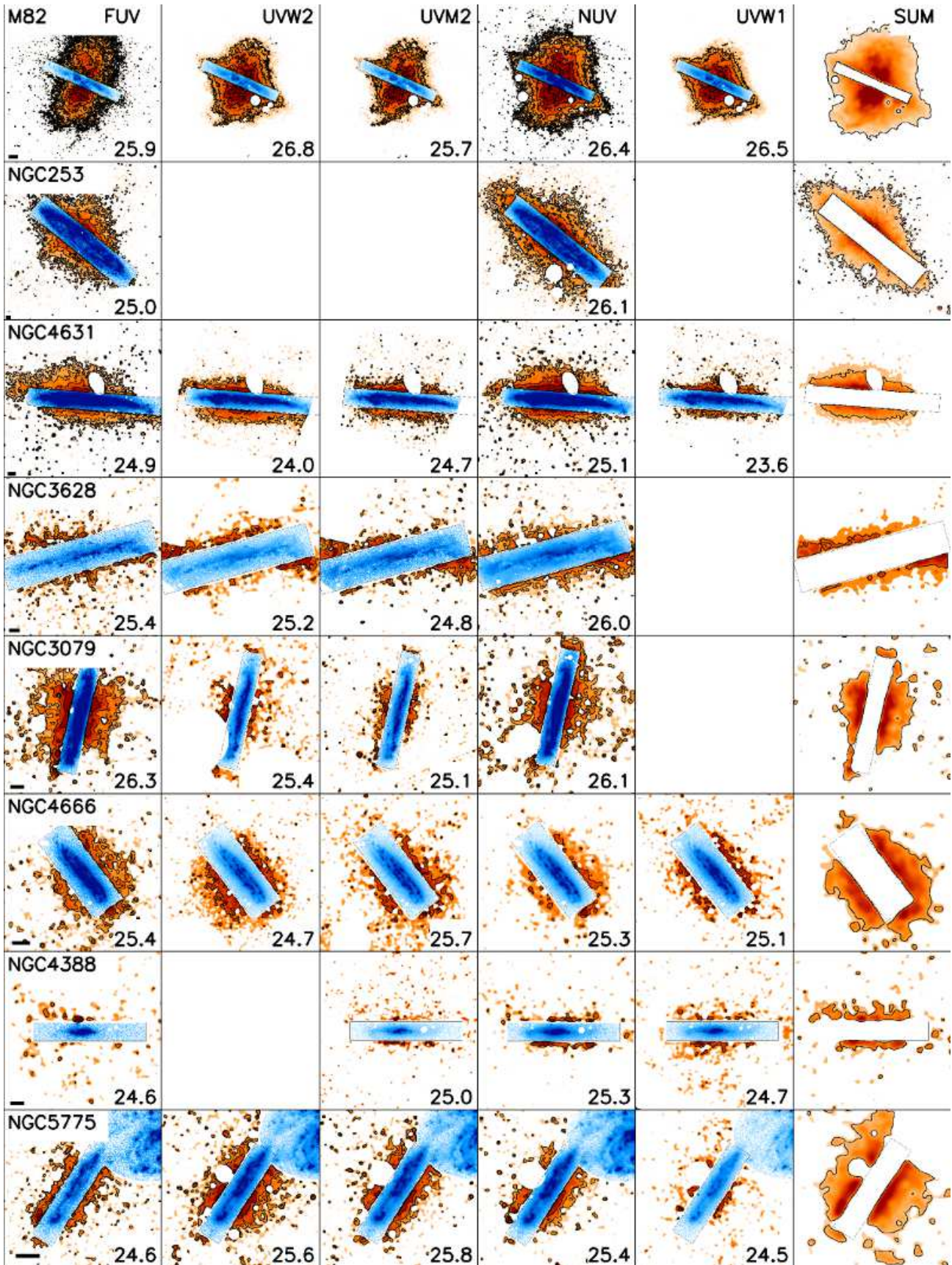


FIG. 4.— UV halos (orange) around starburst galaxies. The format is the same as in Figure 3.

NGC 253, NGC 3079, NGC 3628, NGC 4666, and NGC 5775), as well as two normal galaxies (NGC 4522, NGC 4330). The filaments in the latter two are associated with gas stripped by ram pressure in the Virgo cluster. We cannot rule out the presence of filaments in non-stripped normal galaxies, but those galaxies with high  $S/N$  images do not have filaments.

*Concentration*— The UV halos differ in extent, both in galactocentric radius and projected height. For example, in NGC 891, NGC 2683, and NGC 3044 most of the light is concentrated near the center of the galaxy (Figure 3), whereas in NGC 4216 or NGC 5907 the surface brightness is comparable across most of the disk. We examined the degree of concentration by dividing the UV halo at the midplane and projected galactic center into four quadrants, which were summed. Figure 5 shows the resulting images. Each panel has dimensions of  $2R_{25} \times 2R_{25}$ , where we use the HyperLeda values for  $R_{25}$ . The final two panels show the sum of all of the normal and starburst galaxies, respectively, where the images were reprojected and stacked on a common axis relative to  $R_{25}$ . We excluded the stripped galaxies NGC 4330 and NGC 4522 from this stack.

There are two aspects to the concentration: the extent of the light (as measured by the  $3\sigma$  contour in Figure 5) and its distribution. Among the UV halos of normal galaxies, 6/18 extend in the radial direction to  $R_{25}$  and only one (NGC 4522) extends beyond  $0.5R_{25}$  in the vertical direction. In contrast, all of the starburst halos (8/8) extend to  $R_{25}$  in the radial direction, and 6/8 extend to  $0.5R_{25}$  in the vertical direction. In terms of distribution, for most normal galaxies the UV light is brightest and most vertically extended above the galactic center, with a modest decline with increasing galactocentric radius. This is consistent with a disk-like structure. The starburst galaxies other than NGC 4631 are also less concentrated and filamentary structure at larger heights is superimposed. The similarity in sensitivity and distance between several of the starburst and normal galaxies (e.g., NGC 3079 and NGC 5907) indicates that UV halos are intrinsically brighter and more morphologically complex around starburst galaxies.

When compared to near-IR images, the radial extent of the UV halo along the major axis (relative to  $R_{25}$ ) is unrelated to the prominence of the bulge, so it is unlikely that the radially concentrated UV halos are merely light from the bulge outskirts. The radial or vertical concentration is also unrelated (within each subsample) to the total halo luminosity. The radial concentration also appears to be unrelated to the vertical concentration, and the normal galaxies appear to span a narrow range in vertical extent below  $R_{25}$ .

*Bilateral Symmetry*— We determined the degree of bilateral symmetry by folding images across the midplane. Most galaxies show some asymmetry, although in most cases the visible structure is symmetric while the flux is not, which could be a function of the inclination angle. Among the normal galaxies the bilateral asymmetry is only pronounced for NGC 134, NGC 4330, and NGC 4522, which are experiencing ram-pressure stripping (Kenney & Koopmann 1999; Abramson et al. 2011). Among the starburst galaxies there is asymmetry

in the filamentary structures, but overall the halos are nearly symmetric. An exception is NGC 4631, in which the northern part of the halo is somewhat more extended. NGC 3628 is not bilaterally symmetric, but its halo appears to be warped; if we invert the image along the axis of the midplane, it becomes nearly symmetric. A hint of a similar warp can be seen in the combined image of NGC 4388.

#### 4.3. FUV–NUV Color

In addition to structures visible in each band, we looked for spectral structure in the UV halos. In regions where the halo is detected in all five filters we can construct SEDs, but most galaxies in the sample do not have enough data. Thus, we adopt the FUV–NUV color as a proxy. Figures 6 and 7 show the FUV–NUV color in regions where the flux is detected at  $2\sigma$  above background in each filter for normal and starburst galaxies, respectively. In these images, the smoothing kernel is usually larger than in Figures 3 and 4. The colorbar in the plots is such that blue regions correspond to a blue spectrum (small FUV-NUV) and red regions correspond to a red spectrum (large FUV-NUV). However, values at the edges are not reliable as they are sensitive to the background subtraction (e.g., the red boundaries on the halo of NGC 55 in Figure 3).

There is no obvious structure in the FUV–NUV color maps for most normal galaxies. There appears to be a tendency for the Sc-type galaxies (NGC 5907, NGC 4522, NGC 4330, and NGC 3044) to have bluer halos than the rest (which are Sb, except for NGC 55), but the strength of this connection cannot be assessed with the current sample. This is especially true since NGC 4522 and NGC 4330 are being stripped of their gas by ram pressure from the Virgo intracluster medium. For galaxies where the  $S/N$  is reasonably high across the disk (NGC 55, NGC 891, NGC 4217, and NGC 4330), the color does not change much across with projected galactocentric radius. However, in the starburst galaxies the filaments and regions associated with galactic winds are bluer than the rest of the halo. The underlying FUV-NUV color differs between galaxies, with NGC 3628 and NGC 4388 having generally redder halos; both of these galaxies are classified as Sb type, whereas the others are Sc or Sd. Combined with the normal galaxies, this suggests that bluer galaxies tend to have bluer halos, but the sample size is small. In M82 the FUV-NUV color tends to decrease with height, but the filamentary structures within the wind that are visible in both the FUV and NUV images do not appear in the FUV-NUV color map. In other words, small UV structures in the wind appear to have the same color as the rest of it. It is also of interest that the bluer regions in the halo of NGC 4631 are asymmetric across the midplane, although both sides are blue in the central region where the wind occurs.

#### 4.4. Multiwavelength Comparison

We compare the diffuse UV halos to diffuse extraplanar light in other bands, as well as the disk emission in the same bands. These include  $H\alpha$ , soft X-rays,  $160\ \mu\text{m}$  emission, radio continuum (at 1.4 or 4.8 GHz) and 21 cm emission from neutral hydrogen. The  $H\alpha$  traces the diffuse ionized gas in and above the disk, and the presence

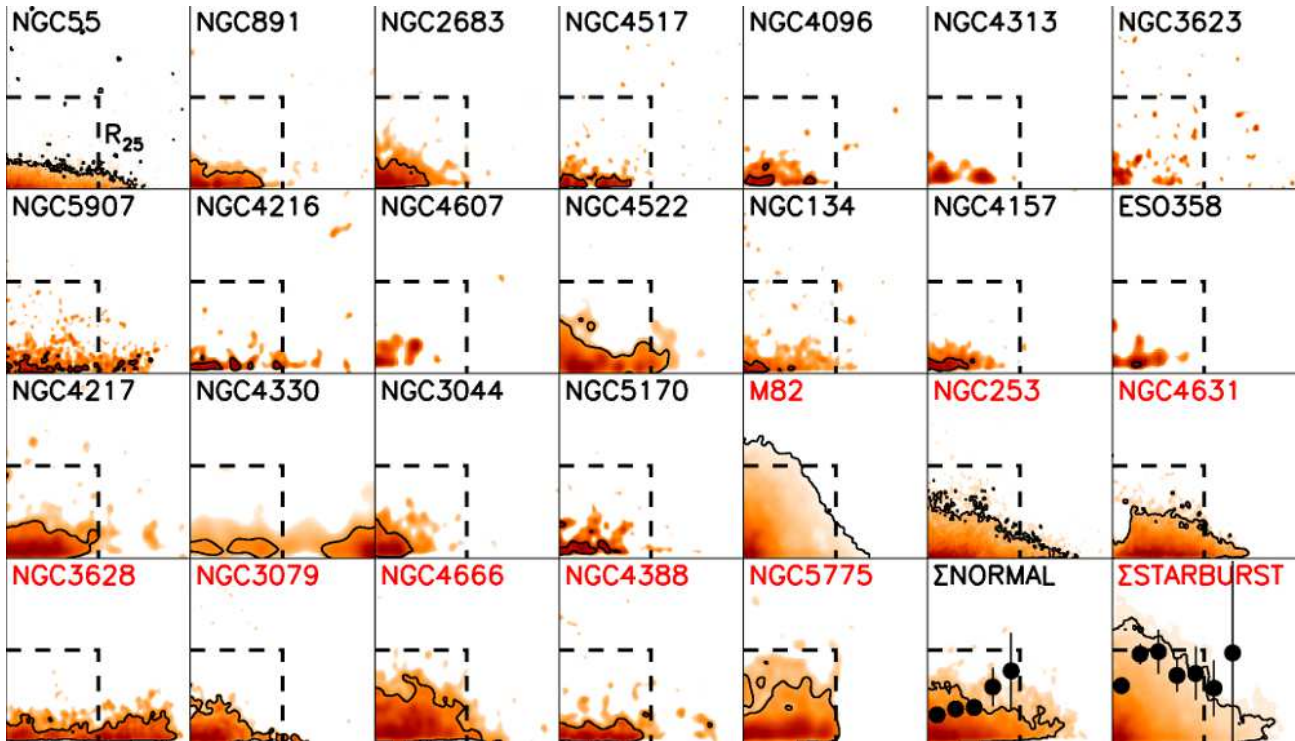


FIG. 5.— Combined images from each filter stacked in the first quadrant and shown relative to the optical radius,  $R_{25}$ . The contour represents the combined  $3\sigma$  threshold above background, and the dimensions of each image are  $2R_{25} \times 2R_{25}$ . The dashed lines show  $R_{25}$ . Starburst galaxies are labeled with red names. The final two panels show the combined normal and starburst galaxies, respectively, with scale heights measured as a function of galactocentric radius shown as points. The “normal” stack excludes NGC 4330 and NGC 4522, which are being stripped by ram pressure. The dip at the center of NGC 4631 is due to masking a satellite galaxy, but it is accounted for in the starburst stack and does not cause the central dip in the scale height there.

of extraplanar diffuse ionized gas (eDIG) indicates disk porosity and ongoing star formation (it may also produce UV emission nebulae through ionized helium). We use  $H\alpha$  images from several atlases (Lehnert & Heckman 1996; Rand 1996; Collins et al. 2000; Rossa & Dettmar 2003b). Diffuse soft X-rays trace hot gas, and X-ray halos seen near the disk are primarily from outflows connected to star formation (Li & Wang 2013). Within the disk, some of the X-rays also come from X-ray binaries. We use X-ray data from the *Chandra* and *XMM-Newton* archives, and the presence of X-ray halos is determined from the literature (Strickland et al. 2004; Tüllmann et al. 2006; Li & Wang 2013). The  $160\mu\text{m}$  images trace thermal emission from dust, and we obtain them from the *Herschel* archive. We use  $160\mu\text{m}$  because it is near the expected peak of the modified blackbody curve for thermal emission, and the spatial resolution at longer wavelengths is considerably worse. The  $160\mu\text{m}$  images are dominated by the disk and the PSF is about 6 arcsec, so we adopt the same approach to clean the overlapping Airy patterns and isolate extraplanar emission (except in NGC 4522). We use the PSF from Aniano et al. (2011), and in some cases the galaxy box is smaller than for the UV. We also refer to McCormick et al. (2013) regarding extraplanar polycyclic aromatic hydrocarbon (PAH) emission and Howk & Savage (1997) and Howk & Savage (1999) for the presence of extraplanar dust seen in absorption as filaments in the optical band. The radio continuum emission comes from cosmic rays produced in supernova remnants, which diffuse out of the disk. We primarily

refer to data taken as part of the CHANG-ES program (Wiegert et al. 2015), but some images come from prior atlases (especially Condon 1987). Finally, we use or refer to high resolution 21 cm maps from a variety of papers (Weliachew et al. 1978; Haynes et al. 1979; Irwin et al. 1987; Irwin 1994; Yun et al. 1994; Lee & Irwin 1997; Kenney & Koopmann 2001; Walter et al. 2004; Oosterloo et al. 2007; Chung et al. 2009; Zschaechner et al. 2012; Westmeier et al. 2013; Yim et al. 2014; Allaert et al. 2015; Lucero et al. 2015; Vollmer et al. 2016). These maps often show filaments of cold gas or warped disks.

$H\alpha$ , soft X-rays, thermal dust emission, and the radio continuum are associated with ongoing star formation, whereas H I need not be. Figures 8 and 9 show the UV contours from above overlaid on  $H\alpha$ , X-ray,  $160\mu\text{m}$ , radio continuum, and 21 cm images for normal and starburst galaxies, respectively. In some cases there is no publicly available data, but we can usually rely on images in the literature (this is especially true for 21 cm data). Galaxies are not included in these figures if they do not have publicly available FITS files in at least two bands. As with the UV images, the  $S/N$  is variable among the galaxies and bands, which limits the power of this comparison.

*Extraplanar Diffuse Emission: Frequency*— About 40% of non-starburst galaxies have eDIG (Rossa & Dettmar 2003a), and a similar number of galaxies in our sample with data from these bands (Table 6) have eDIG (38%), radio (45%), or soft X-ray halos (40%). However, 67%

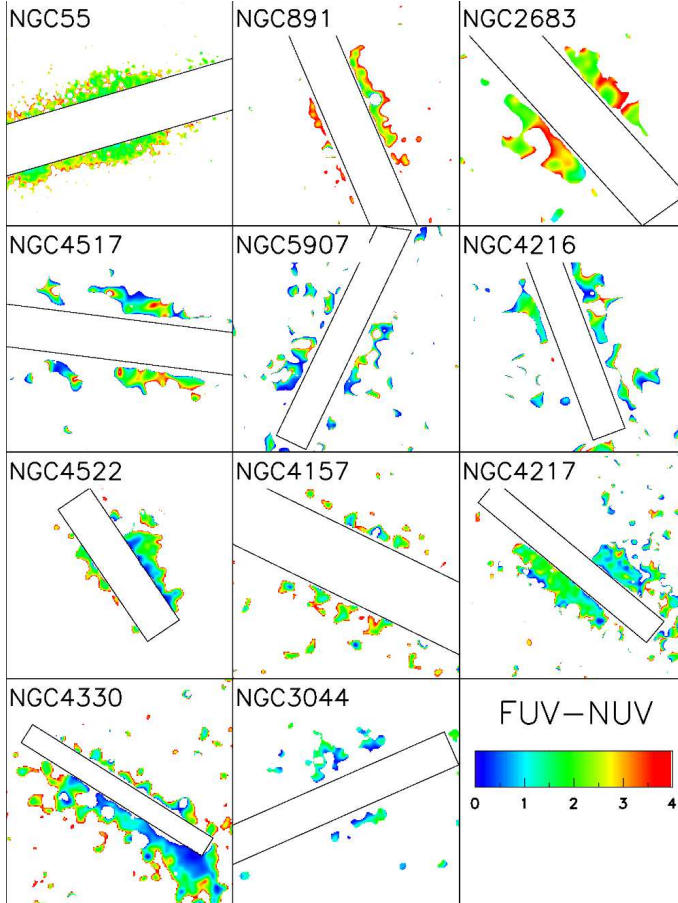


FIG. 6.— The FUV–NUV color (per square arcsec) for normal galaxies. The FUV and NUV images used to create these maps were smoothed and clipped at the mutual  $2\sigma$  level (i.e., where emission is detected at  $2\sigma$  above background in each image). The *GALEX* pixel size is 1.5 arcsec.

of galaxies with  $160\ \mu\text{m}$  images have extraplanar emission (sometimes at lower heights than the UV halos; Figure 8). The sample overlap with McCormick et al. (2013) is not large enough to determine the fraction with extraplanar PAH emission. In contrast, UV halos are seen around every normal galaxy. Several of the galaxies in our sample were also investigated by Howk & Savage (1997) and Howk & Savage (1999), who used unsharp mask images in the optical to identify high latitude dust absorption. These include NGC 891, NGC 4517, NGC 4565, NGC 5907, NGC 4217, and NGC 4157, of which NGC 891 and NGC 4217 have high latitude dust. The starburst galaxies all have eDIG, soft X-ray halos, extraplanar thermal dust emission (except for NGC 3628), and radio halos. H I emission is also seen around all galaxies in the sample with high resolution maps, although in some cases the beamsizes makes it unclear how much of the emission is truly extraplanar.

*Extraplanar Diffuse Emission: Morphology*— The extraplanar diffuse emission in normal galaxies shows some of the same features as the UV halo morphology, although sometimes it is only detected at lower heights where we cannot measure the UV halo morphology directly. The eDIG tends to have a similar morphology as the UV in terms of filaments, concentration, and bilat-

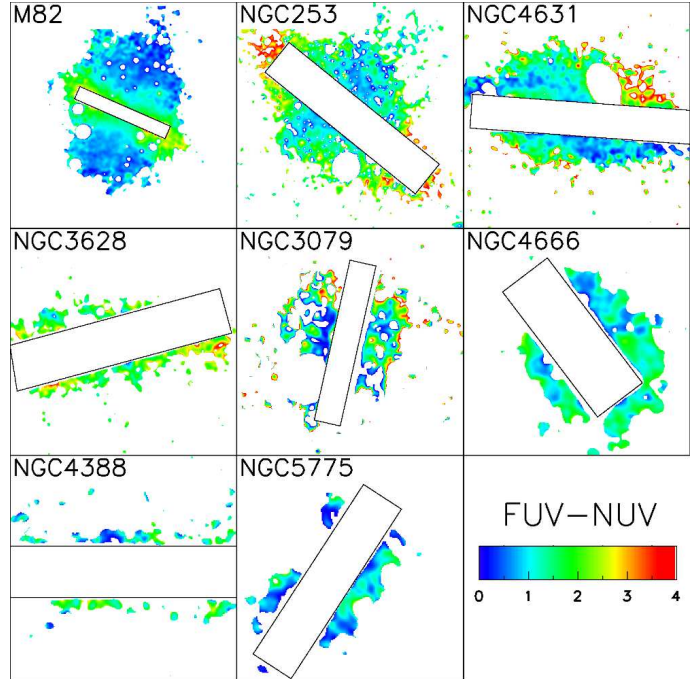


FIG. 7.— The FUV–NUV color for starburst galaxies. The plot style is the same as in Figure 6.

eral symmetry, but it is usually not detected at larger heights where the UV halo remains bright. The soft X-ray halos correspond reasonably well to the UV halo structure in NGC 891, NGC 2683, and NGC 4217, but not in NGC 5170. There are fewer normal galaxies with X-ray data than with  $H\alpha$  images, and only four with X-ray halos, so it is unclear how well the morphology matches the UV. The extraplanar  $160\ \mu\text{m}$  emission coincides with the UV, but it is not always as extensive. NGC 55, NGC 891, and NGC 4096 have the most convincing  $160\ \mu\text{m}$  halos, but their prominence does not appear to be connected to that in  $H\alpha$  or the radio continuum. Likewise, the prominence of the radio halos seems unrelated to the prominence of the UV halo or extraplanar emission in other bands. The only normal galaxies in McCormick et al. (2013) with extraplanar PAH emission are NGC 55 and NGC 891. In the former case, the PAHs do not follow the UV halo, whereas in the latter they do. NGC 891 and NGC 4217 have high latitude dust seen by Howk & Savage (1999). Although these two galaxies do have brighter UV halos than others in the Howk & Savage (1999) sample, the UV halos in the four galaxies without high latitude dust absorption have about the same vertical extent and radial concentration.

Starburst UV halos have filamentary structure that is also seen at other wavelengths. This is especially true in  $H\alpha$ , although a similar pattern is seen in X-ray and radio halos. There are some disagreements in extraplanar morphology among these bands (such as in M82, NGC 4631, or NGC 4388), but there is a clear connection between the UV filaments and those seen at other wavelengths. The same is true for the extraplanar dust emission, although not every filament is associated with  $160\ \mu\text{m}$  emission. However, unlike at other wavelengths the UV halos span the disks of the starburst galaxies, and this non-filamentary structure is not present in  $H\alpha$ , X-rays,

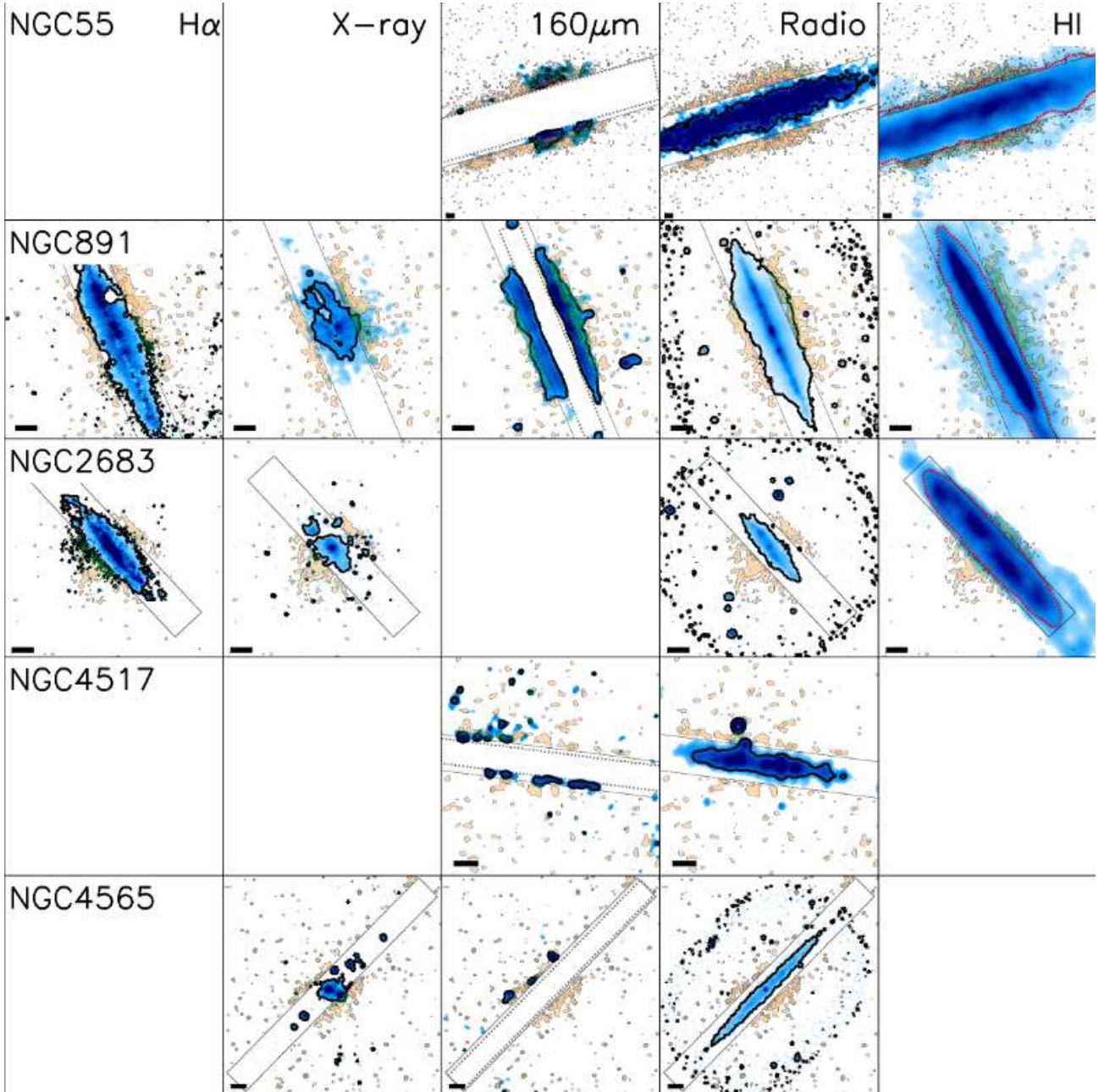


FIG. 8.— A comparison of the UV halos to diffuse emission in other bands for normal galaxies. Empty panels indicate where we have no image file, but in some cases we can compare the morphology from published images (see Table 2). The orange maps show the FUV (or  $uvw2$ ) contours from Figure 3 while the blue maps show images at the other wavebands. The thick black contour is the  $3\sigma$  contour above background for each of these images. The thin black box shows our galaxy region for PSF-wing contamination. To emphasize the extraplanar emission at  $160\mu\text{m}$  we also corrected these images for PSF-wing contamination, and the dotted lines show the galaxy regions used. In some images the map edges are visible as regions of heightened noise, and the contours there should be ignored.

thermal dust emission, or radio continuum. In general the PAHs do not follow the UV halos (McCormick et al. 2013). Some of the same filaments are visible in PAHs, but the coincidence of UV and PAH filaments is worse than at other wavelengths, and the diffuse components above the disk have different shapes.

The connection between the 21-cm morphology and the UV halos is unclear. We note that the sensitivities and resolutions of the H I images in Figure 9 differ, so the  $N_{\text{H}} = 5 \times 10^{20} \text{ cm}^{-2}$  contour (assuming optically thin hydrogen) is shown as a shorthand for the

transition from disk to halo gas. The H I and UV morphology are similar for the galaxies undergoing ram-pressure stripping (NGC 134, NGC 4522, NGC 4330, and NGC 4388). The galaxies in the Virgo cluster also tend to have less extensive extraplanar H I, but there is no clear difference between the UV halos of the Virgo galaxies (NGC 4313, NGC 4216, NGC 4330, NGC 4607, NGC 4522, NGC 4217, NGC 4388, and NGC 5775) and the others. There is also no apparent connection between the UV halo morphology and H I warps, or between the vertical concentration in the H I total column maps and

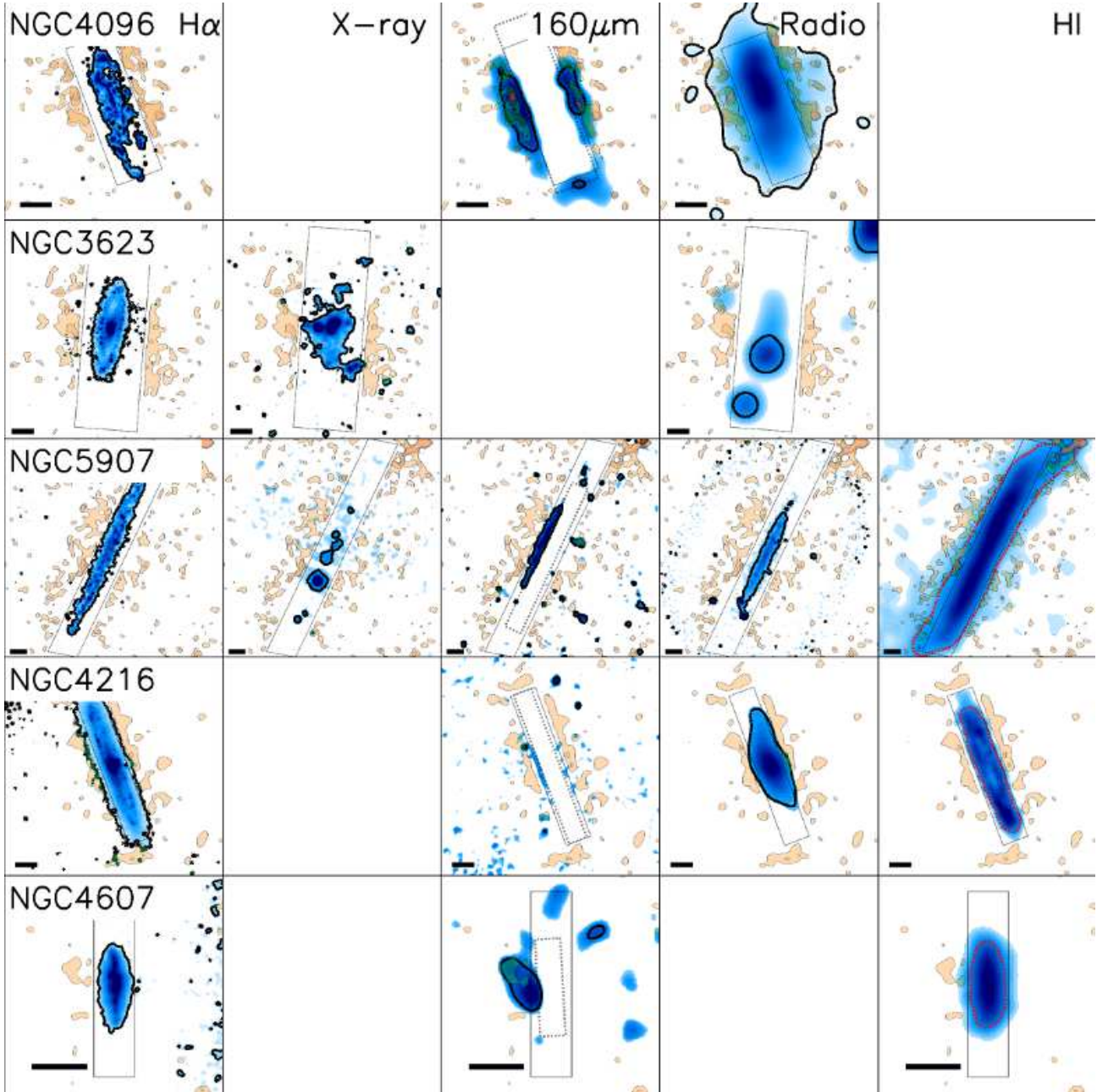


FIG. 8.— continued

the diffuse UV images.

The UV and HI filaments do coincide near the disk in the starburst galaxies NGC 253, NGC 3628, NGC 4666, NGC 5775, and NGC 3079 (not all shown in Figure 9). The UV halo is also brighter and more vertically extended on the side of the galaxy with the large HI filament in NGC 891, and a similar phenomenon is seen in NGC 3044. However, the large-scale hydrogen filaments seen around galaxies in our sample (such as NGC 55, NGC 3628, NGC 4565, NGC 4631, or M82) are not visible in the UV.

*Disk Emission*— There is good agreement in most normal galaxies between the projected radial extent (along the disk) of the bright H $\alpha$  disk emission and the UV

halo above it, which mostly explains the difference in UV halo concentration among normal galaxies. The same is true for soft X-rays, radio continuum, and thermal emission from dust in the disk, except for NGC 4565 and NGC 4522 (Figure 8). In the starburst galaxies, the disk emission is less connected to the UV halo and is instead brightest in the regions where the galactic winds occur.

#### 4.5. Summary

UV halos around luminous spiral galaxies are ubiquitous. In normal galaxies, the UV halos tend to form a thick disk. Their presence is independent of diffuse extraplanar material seen in other wavebands, but in those cases where a diffuse extraplanar layer does exist, it has a similar morphology to the UV halo and occurs in

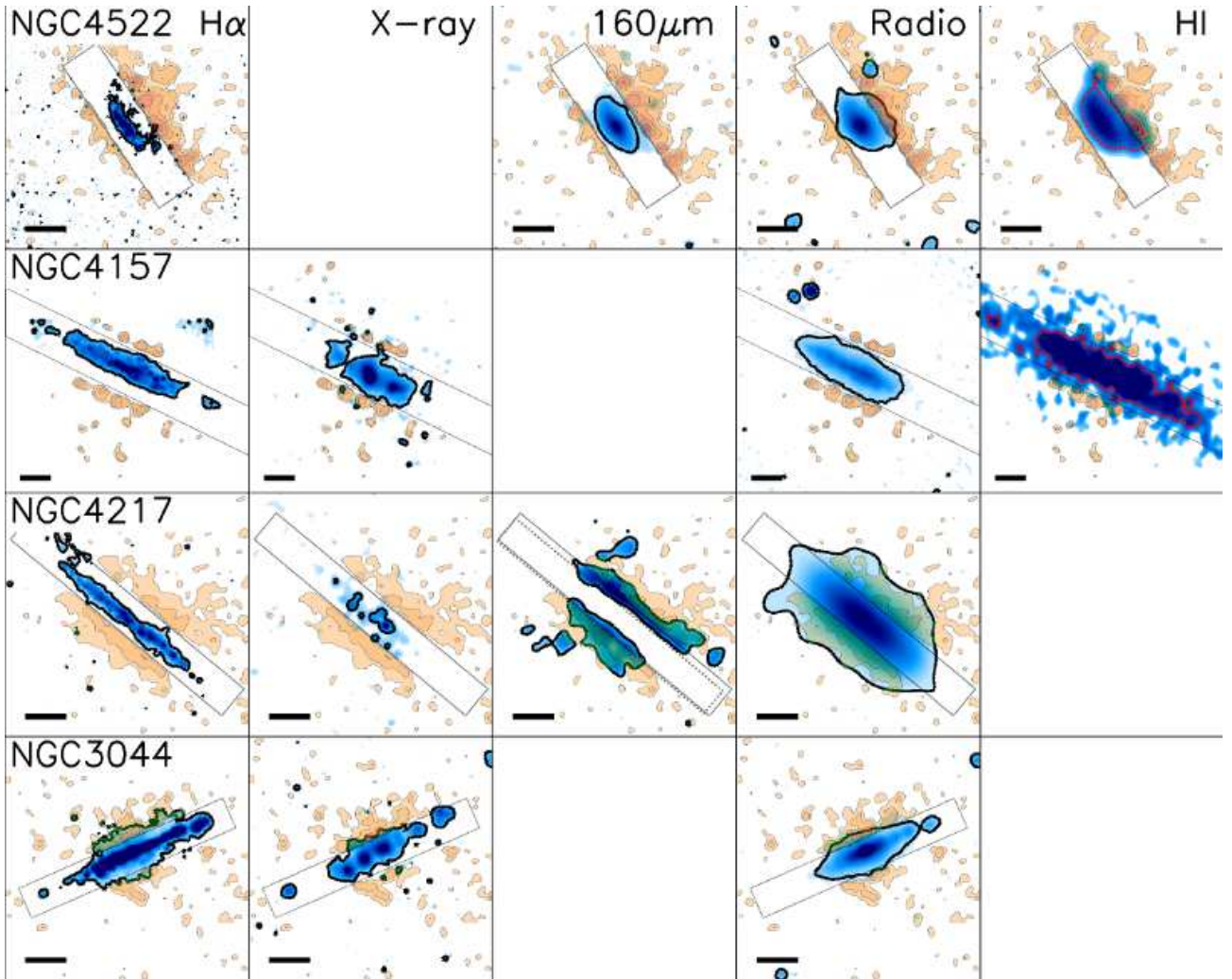


FIG. 8.— continued

about the same place. This suggests that the UV halos arise from some gaseous medium, which is supported by the asymmetric halos in NGC 4522 and NGC 4330 that match the morphology of the stripped gas, but not the morphology of the stellar disk. The FUV–NUV colors differ between galaxies, but there are no clear structures in the FUV–NUV colors, except perhaps in stripped galaxies. The UV halos do appear to be connected to star formation in the disk, as they are brightest over the parts of the disk with bright H $\alpha$ , X-ray, or radio emission, but not in a way that requires ionizing photons or winds to escape the disk.

UV halos around starburst galaxies are more extended and have filamentary structures coincident with the galactic winds. Apart from these filaments, there is little agreement between the extraplanar or disk emission in other wavebands. The winds are visible in the FUV–NUV maps as bluer regions in the UV halo, and may be superimposed on a disk structure like that in the normal galaxies, but the origin of the color difference is not clear.

## 5. ULTRAVIOLET HALO FLUXES

In the prior section we focused on qualitative morphological trends. Here we compare the average halo fluxes and FUV–NUV colors, as well as the flux as a function of height above the disk, to various metrics for each galaxy. It is especially important to understand the connection between the structure visible in the UV maps and the average properties because it will not be possible to observe this structure with reasonable exposure times for more distant galaxies.

We measured halo UV fluxes in long boxes parallel to the midplane of the galaxy, as in HKB14. The length of each box is equal to the length of the region containing the galaxy image, and the width of each box is a projected 2 kpc at the distance of the galaxy. We also reference the height of the box to the projected midplane of the galaxy. For galaxies with lower inclinations, such as NGC 4666, the projected heights are too large. The halo fluxes are all measured starting from a projected height of 2–5 kpc from the midplane in our sample. This conservative threshold excludes galaxy disk light, but likely misses halo light at lower latitudes. The galaxy fluxes measured in the boxes used for PSF-wing correction are reported in Table 4.

The halo fluxes are corrected for PSF-wing contam-

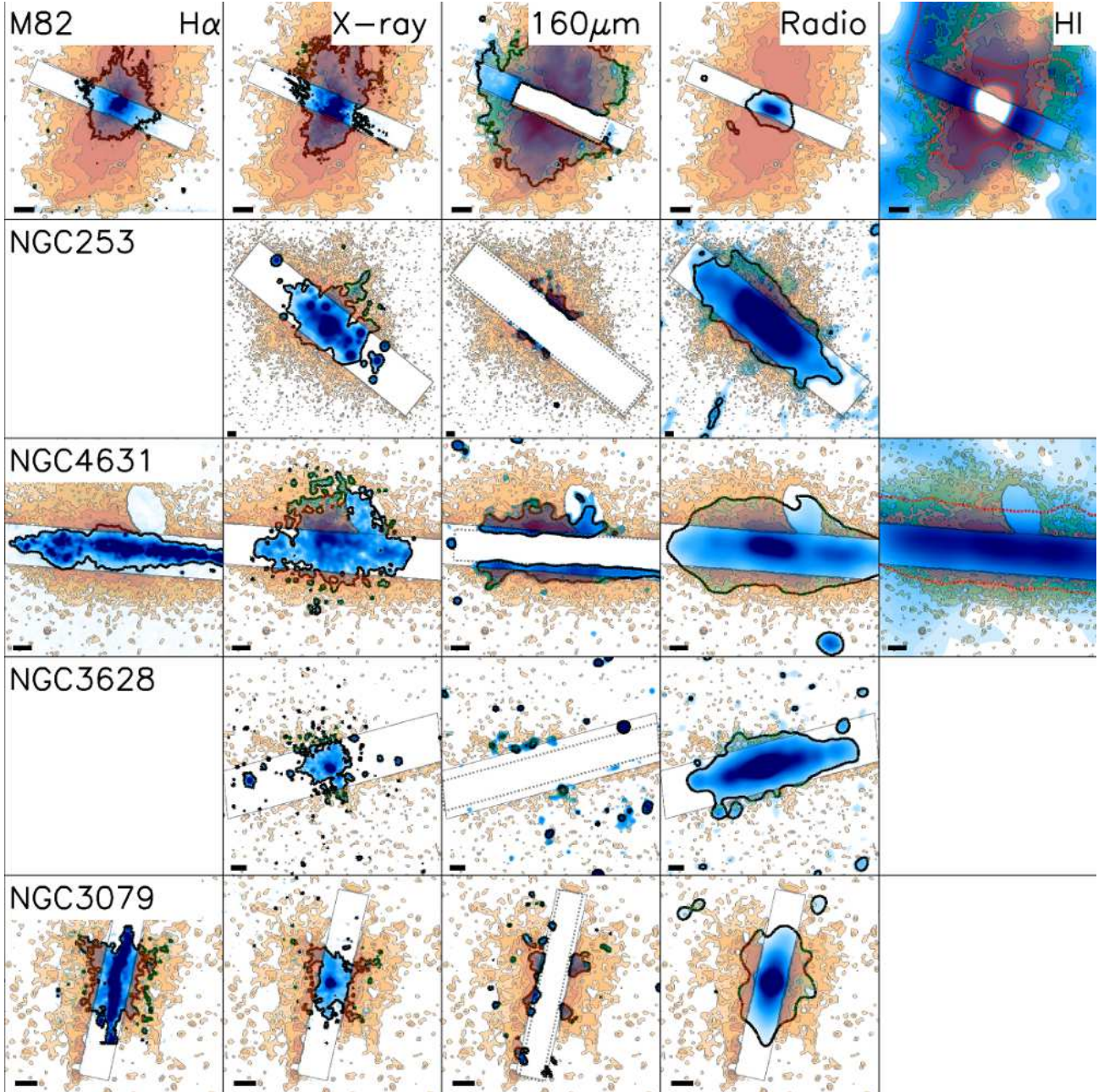


FIG. 9.— A comparison of the UV halos to diffuse emission in other bands for starburst galaxies. The plot style is the same as in Figure 8.

ination, and the *uvw2* fluxes are corrected for the red leak using a galaxy-type correction from HKB14 to isolate the true UV flux (shortward of  $3000\text{\AA}$ ). We used a correction factor of 0.93, except for M82 (0.95) and NGC 3623 (0.85). The *uvw1* filter has a more severe red leak for which this correction is unreliable, so we report the uncorrected fluxes. The total halo fluxes, amount of PSF-wing contamination, and *uvw2* correction factors are listed in Table 5.

In the remainder of this section, we assess the reliability of the measured fluxes, measure scale heights for the UV halos, and examine the change in color as a function of height. We then search for correlations between the average UV halo fluxes and galactic properties, and compare our results to HKB14.

### 5.1. Reliability of Halo Fluxes

The similarity in the halo morphology between different UV filters suggests that our PSF-wing subtraction is accurate, but it is worth considering the reliability of the measured fluxes when the PSF-wing contamination can be a large fraction of the total flux. We performed several tests, and conclude that the fluxes are indeed reliable in the sense that the systematic error from PSF-wing subtraction is smaller than the statistical error.

First, the PSF-wing contamination is not very sensitive to the best-fit exponent because most of the PSF-wing contamination comes from the region where the profile is measured rather than extrapolated. If we extrapolate the PSFs with an exponent of  $x = 2$  in each filter, which



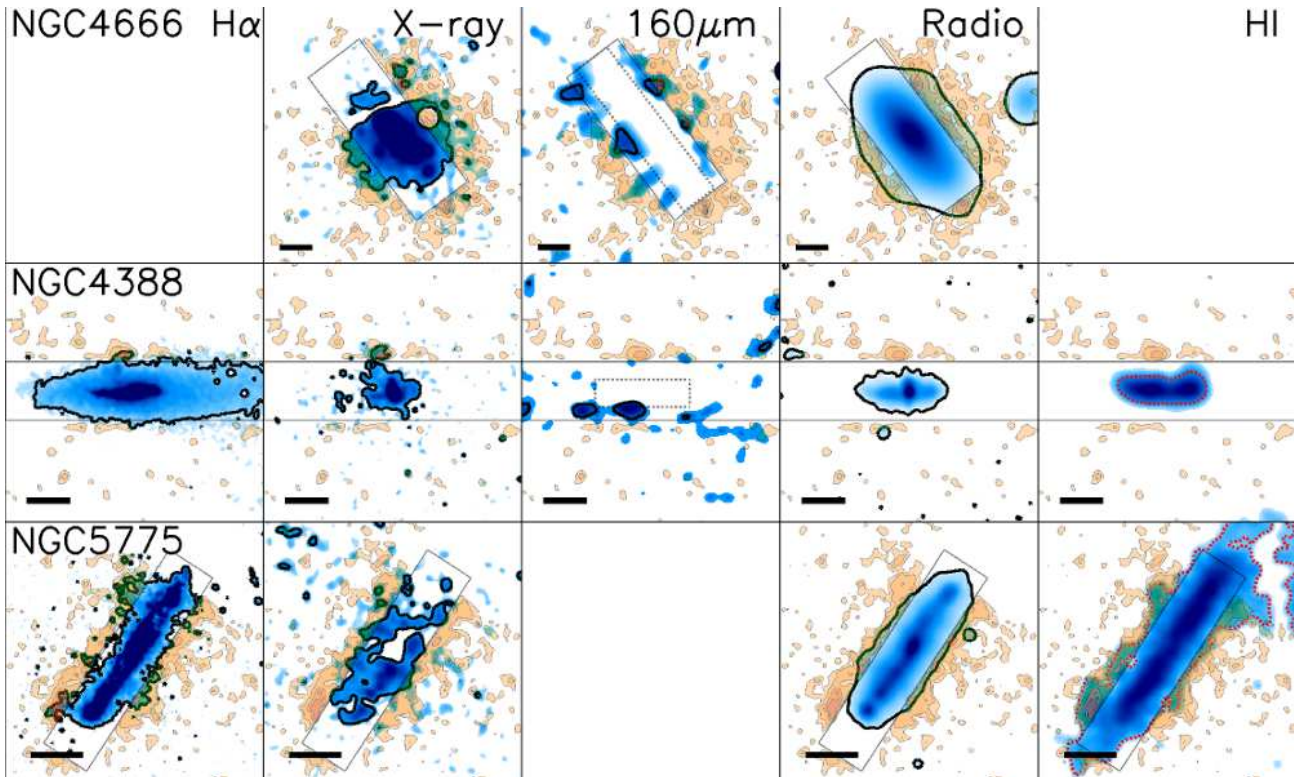


FIG. 9.— continued

is unacceptably shallow (Table 3) and inconsistent with the background, the fractional increase in the PSF-wing contamination is only about 2%, except in the *uvw1* filter where the change is about 8%.

Second, the NUV filter covers approximately the same wavelength range as the combined *uvm2* and *uvw1* filters. Since the PSF-wing contamination is smaller in the NUV, comparing the NUV fluxes to the average of the *uvm2* and *uvw1* can tell us if the PSF-wing contamination is obviously too high or low. For galaxies with fluxes in each filter we measured the flux with and without accounting for PSF-wing contamination, and averaged the *uvm2* and *uvw1* values. Without the PSF-wing correction, the mean UVOT/*GALEX* flux ratio is about 1.6 across our sample, whereas after correction it is about 1.05. We cannot exactly synthesize the NUV filter from the UVOT filters, so a ratio of 1.0 is not expected and this comparison cannot tell us if there are small systematic uncertainties. Nonetheless, this exercise suggests that the reported fluxes are close to the true flux.

Finally, there are *HST* observations of the halo of M82 in several UV bands (using the Wide Field Camera 3 UVIS detector), including the F225W filter that overlaps with the *uvw2*, NUV, *uvm2*, and *uvw1* filters. The sub-arcsecond angular resolution and small field of view mean that PSF-wing contamination is negligible. The wind is clearly visible in the *HST* image, and the flux measured in this region is consistent with that measured with *Swift* and *GALEX* after PSF-wing subtraction but not before. For example, in one region (a circle of radius 15 arcsec centered on  $\alpha = 09:55:52.22$ ,  $\delta = +69:40:02.39$ ), we measure an AB magnitude of  $m_{F225W} = 16.91 \pm 0.04$  mag in the *HST* image,  $m_{uvm2} = 16.80 \pm 0.03$  mag in the

*uvm2* image before PSF-wing correction, and  $m_{uvm2} = 16.92 \pm 0.03$  mag after. Similar values are found in the other filters, indicating that the PSF-wing subtraction recovers the true flux to within the statistical uncertainty.

## 5.2. Scale Heights

UV halos appear to have a morphology like a thick disk, so we measured scale heights ( $h$ ) based on fitting a function of the form  $F(z) = Ae^{-|z|/h}$ , where  $F$  is the flux,  $A$  is a normalization, and  $z$  is the projected height above the midplane. We used the fluxes measured in long boxes because the  $S/N$  is only high enough in a few galaxies to measure scale heights at different radii. To see how the aggregate behaves, we fit scale heights at several galactocentric radii in the stacked quadrant images. Figure 5 shows the scale height as a function of galactocentric radius, along with the  $1\sigma$  error bars, for the normal and starburst galaxies. In the starburst galaxies the source mask near  $R = 0$  for NGC 4631 is taken into account. In the normal galaxy stack the scale height within  $R_{25}$  is consistent with being constant, with a possible increase with larger radii that may be due to a more complex background that results from the stacking. The starburst stack shows that the scale height changes with galactocentric radius, which can be explained by filaments. The scale heights can also differ between filters, as is the case for M82 and NGC 253, but in most galaxies the scale heights measured in different filters agree within the uncertainty. Here we report the value of  $h$  measured from the average radial profile and combining each filter (we allowed  $A$  to vary between filters, but fit for a common  $h$ ). Table 6 contains the best-fit  $h$  and the

TABLE 4  
GALAXY UV FLUXES

Name (1)	FUV (2)	NUV (3)	<i>uvw2</i> (4)	<i>uvm2</i> (5)	<i>uvw1</i> (6)	<i>uvw2</i> Factor (7)
Starburst Galaxies						
NGC0253	105.20 ± 0.01	200.78 ± 0.02				0.93
M82	3.67 ± 0.04	17.30 ± 0.08	14.47 ± 0.09	13.49 ± 0.07	37.96 ± 0.04	0.95
NGC4631	92.80 ± 0.06	132.3 ± 0.1	108.4 ± 0.2	121.3 ± 0.3	132.6 ± 0.4	0.93
NGC3628	5.45 ± 0.02	14.6 ± 0.1	11.6 ± 0.1	11.9 ± 0.2	28.3 ± 0.9	0.93
NGC4666	5.69 ± 0.04	10.20 ± 0.04	8.31 ± 0.07	8.20 ± 0.09	13.95 ± 0.08	0.93
NGC3079	10.39 ± 0.01	16.29 ± 0.02	13.96 ± 0.02	16.12 ± 0.04	20.9 ± 0.1	0.93
NGC5775	2.47 ± 0.01	4.48 ± 0.03	4.38 ± 0.01	4.13 ± 0.02	7.36 ± 0.03	0.93
NGC4388	3.16 ± 0.01	6.50 ± 0.01	5.68 ± 0.01	6.36 ± 0.01	9.87 ± 0.02	0.93
Normal Galaxies						
NGC0055	294.56 ± 0.01	441.60 ± 0.03				0.93
NGC0891	2.85 ± 0.06	5.7 ± 0.2	5.5 ± 0.2	4.6 ± 0.3	10.77 ± 0.05	0.93
NGC2683	6.36 ± 0.02	12.35 ± 0.04	10.27 ± 0.04	10.23 ± 0.09	19.9 ± 0.3	0.93
NGC4517	6.39 ± 0.02	10.27 ± 0.03				0.93
NGC4565		15.45 ± 0.01				0.93
NGC4096	7.26 ± 0.03	12.80 ± 0.04	10.39 ± 0.03	11.17 ± 0.03		0.93
NGC4313	0.24 ± 0.01	1.00 ± 0.01				0.93
NGC3623	3.25 ± 0.04	9.58 ± 0.05	7.60 ± 0.03	8.04 ± 0.02	20.66 ± 0.05	0.85
NGC5907	7.99 ± 0.03	12.96 ± 0.05	10.99 ± 0.03	11.58 ± 0.06	16.75 ± 0.04	0.93
NGC4216	1.42 ± 0.02	3.70 ± 0.02				0.93
NGC4607	0.22 ± 0.01	0.60 ± 0.01				0.93
NGC4522	2.57 ± 0.01	4.03 ± 0.02				0.93
NGC0134			10.28 ± 0.05	10.46 ± 0.07	17.4 ± 0.2	0.93
NGC4157	3.13 ± 0.02	9.60 ± 0.04				0.93
ESO358	1.62 ± 0.01	3.30 ± 0.02				0.93
NGC4217	0.74 ± 0.03	1.50 ± 0.03				0.93
NGC4330	1.41 ± 0.01	2.27 ± 0.01	1.87 ± 0.02	1.99 ± 0.02	2.64 ± 0.03	0.93
NGC3044	5.77 ± 0.02	9.30 ± 0.02	6.98 ± 0.04	7.74 ± 0.03	9.56 ± 0.03	0.93
NGC5170	2.40 ± 0.07	5.06 ± 0.04				0.93

NOTE. — The galaxy fluxes are measured in boxes as described in Section 5. The *uvw2* scale factor is based on the galaxy type as described in HKB14.

associated reduced  $\chi^2$ .

Scale heights range from  $h = 1 - 8$  kpc. The mean value of  $h$  for starburst galaxies is  $\bar{h} = 3.6$  kpc (3.0 kpc when excluding NGC 4666, which has a lower inclination), and it is  $h = 3.5$  kpc for normal galaxies. There is no dependence on H $\alpha$  luminosity, the presence of eDIG, Hubble type, UV halo luminosity, or the  $S/N$  in the image. Galaxies with stripped gas (NGC 4522, NGC 134, and NGC 4330) have small scale heights ( $h < 2$  kpc), but NGC 891 and NGC 55 have similar  $h$  values even without stripped gas. Likewise, there is no connection between  $h$  and the fraction of UV light from filaments. The galactic or halo properties that seem to be connected to other morphological indicators of UV halos do not predict the scale height.

In several galaxies,  $h$  varies between filters. For example, in NGC 253 the joint fit to all filters results in  $h = 2.2$  but with a reduced  $\chi^2 = 38$ . The FUV profile is marginally fit for  $h = 1.8$  kpc (reduced  $\chi^2_\nu = 2$ ), but the NUV profile cannot be fit with a single exponential profile ( $h = 2.6$  kpc with reduced  $\chi^2 = 43$ ). A double exponential profile is a good fit with an inner component ( $h \approx 1$  kpc) and an outer component ( $h \approx 3$  kpc), so it is possible that the NUV light has a compact component and a component similar to the FUV halo. Figure 4 shows that the NUV light follows the disk much better than the FUV light, suggesting a possible difference in physical origin. A similar difference is found in M82, where the joint fit produces  $h = 2.7$  kpc ( $\chi^2_\nu = 32$ ) and the best-fit values of  $h$  in each filter are:  $h = 4.9, 3.0,$

$2.9, 3.2,$  and  $2.5$  kpc for the FUV, *uvw2*, *uvm2*, NUV, and *uvw1* filters, respectively (with corresponding  $\chi^2_\nu = 1.7, 4.4, 0.8, 2.9,$  and  $12$ ). As in NGC 253, the FUV halo is more extended, and the redder filters cannot be adequately described by single exponential models. On the other hand, in NGC 55 (joint  $h = 1.1$  kpc and  $\chi^2_\nu = 4.2$ ) the FUV halo has a smaller scale height than the NUV ( $h \approx 0.5$  kpc compared to 1.3 kpc). It is tempting to ascribe the difference in behavior to the presence of galactic winds, and indeed NGC 3079, NGC 4631, and NGC 4666 do have shallower FUV than NUV profiles, but the  $S/N$  is generally too low in the normal galaxies to determine if this is a clear difference between them.

We also searched for different scale heights across the midplane. In many cases, one filter has a different profile across the midplane while the others do not, but these can usually be explained by a small background gradient across the region of the galaxy (e.g., due to Galactic cirrus, which differs in strength between filters). The exception is M82, where the FUV markedly differs across the midplane in a way that other filters do not. The most likely explanation is that the wind is brightest in the FUV, as seen in Figure 7. Most galaxies have approximately symmetric flux profiles, despite differences in the visible morphology across the midplane (e.g., Figure 4). The galaxies where there is a notable difference in multiple filters include NGC 4666, NGC 4522, NGC 4330, and NGC 134. The latter three galaxies have an obvious asymmetry due to stripped gas (Figure 3). NGC 4666 is the least inclined galaxy in the sample, and the asym-

TABLE 5  
 HALO UV FLUXES

Name (1)	FUV (2)	NUV (3)	Halo Flux (mJy)			PSF-Wing Contamination (mJy)					<i>uvw2</i> Factor (12)
			<i>uvw2</i> (4)	<i>uvm2</i> (5)	<i>uvw1</i> (6)	FUV (7)	NUV (8)	<i>uvw2</i> (9)	<i>uvm2</i> (10)	<i>uvw1</i> (11)	
Starburst Galaxies											
NGC0253	5.43 ± 0.09	17.2 ± 0.2				4.89	0.60				0.93
M82	7.0 ± 0.1	15.7 ± 0.2	14.4 ± 0.2	13.3 ± 0.2	25.9 ± 0.1	0.29	0.53	0.69	0.54	2.94	0.95
NGC4631	2.74 ± 0.07	5.3 ± 0.2	5.0 ± 0.3	5.0 ± 0.4	6.20 ± 0.5	5.75	0.99	3.16	3.01	6.39	0.93
NGC3628	0.46 ± 0.01	1.92 ± 0.09	1.4 ± 0.1	1.2 ± 0.1	3.3 ± 0.4	0.20	0.11	0.21	0.19	0.80	0.93
NGC4666	0.23 ± 0.02	0.51 ± 0.02	0.49 ± 0.03	0.36 ± 0.04	0.48 ± 0.04	0.16	0.06	0.13	0.11	0.39	0.93
NGC3079	0.42 ± 0.01	0.65 ± 0.02	0.65 ± 0.05	0.63 ± 0.04	0.5 ± 0.1	0.53	0.23	0.43	0.41	1.15	0.93
NGC5775	0.23 ± 0.01	0.39 ± 0.02	0.49 ± 0.01	0.40 ± 0.01	0.71 ± 0.03	0.13	0.11	0.17	0.14	0.45	0.93
NGC4388	0.12 ± 0.01	0.37 ± 0.01	0.25 ± 0.01	0.29 ± 0.01	0.90 ± 0.02	0.14	0.08	0.16	0.14	0.49	0.93
Normal Galaxies											
NGC0055	1.0 ± 0.2	12.6 ± 0.8				13.99	0.51				0.93
NGC0891	0.58 ± 0.05	0.8 ± 0.2	0.8 ± 0.1	1.0 ± 0.3	1.3 ± 0.2	0.15	0.05	0.15	0.10	0.47	0.93
NGC2683	0.30 ± 0.02	0.88 ± 0.04	0.84 ± 0.04	0.5 ± 0.1	1.6 ± 0.4	0.29	0.11	0.28	0.22	0.94	0.93
NGC4517	0.23 ± 0.02	0.9 ± 0.4				0.33	0.12				0.93
NGC4565		1.08 ± 0.09					0.17				0.93
NGC4096	0.10 ± 0.02	0.48 ± 0.04	0.54 ± 0.03	0.41 ± 0.02		0.34	0.18	0.31	0.27		0.93
NGC4313	0.05 ± 0.01	0.12 ± 0.02				0.01	0.03				0.93
NGC3623	0.02 ± 0.02	0.21 ± 0.03	0.19 ± 0.02	0.17 ± 0.01	0.47 ± 0.03	0.06	0.01	0.07	0.06	0.37	0.85
NGC5907	0.22 ± 0.02	0.43 ± 0.04	0.39 ± 0.02	0.43 ± 0.04	0.42 ± 0.03	0.39	0.10	0.29	0.25	0.77	0.93
NGC4216	0.08 ± 0.01	0.34 ± 0.02				0.07	0.08				0.93
NGC4607	0.02 ± 0.01	0.07 ± 0.01				0.01	0.03				0.93
NGC4522	0.15 ± 0.01	0.25 ± 0.02				0.11	0.09				0.93
NGC0134			0.44 ± 0.03	0.24 ± 0.05	0.6 ± 0.1			0.26	0.21	0.75	0.93
NGC4157	0.15 ± 0.02	0.31 ± 0.01				0.13	0.08				0.93
ESO358	0.06 ± 0.01	0.19 ± 0.02				0.06	0.03				0.93
NGC4217	0.17 ± 0.03	0.50 ± 0.03				0.04	0.06				0.93
NGC4330	0.11 ± 0.01	0.17 ± 0.01	0.20 ± 0.03	0.15 ± 0.02	0.26 ± 0.05	0.08	0.16	0.12	0.11	0.26	0.93
NGC3044	0.11 ± 0.02	0.13 ± 0.01	0.09 ± 0.04	0.10 ± 0.03	0.02 ± 0.05	0.31	0.32	0.29	0.28	0.69	0.93
NGC5170	0.04 ± 0.05	0.67 ± 0.05				0.08	0.09				0.93

NOTE. — The halo fluxes are measured as described in Section 5. The *uvw2* scale factor is based on the galaxy type as described in HKB14. The total flux measured on the CCD is the sum of the inferred astrophysical flux (“halo flux”) and the PSF-wing contamination.

metry in scale heights may pertain to inclination and projection effects, as mentioned in HKB14.

### 5.3. FUV-NUV Color with Height

We measured the correlation between the FUV–NUV color in each flux measurement bin and the projected height of the bin for each galaxy with data in both filters. Most galaxies have no significant correlation (for a threshold of  $p = 0.05$ ), and the exceptions are all starbursts. In NGC 253, M82, NGC 4631, NGC 3628, NGC 3079, and NGC 4388, the FUV–NUV color decreases with height. This is consistent with the FUV–NUV color maps (Figure 7) and suggests that the UV halos comprise two components.

To improve the signal, we measured the FUV–NUV color as a function of height in composites of the normal, starburst, and stripped galaxies (of which NGC 4522 and NGC 4330 have *GALEX* data). The composite measurements are shown in Figure 10. The data were binned in boxes 2 kpc wide, with the first box having a central height of 3 kpc from the midplane. The projected distances from the midplane for each measurement were used to assign each measurement to the appropriate bin, and the galaxies were projected to a common distance of 20 Mpc for the purpose of computing the magnitudes. Figure 10 reinforces the conclusions from the individual galaxies: the starburst halos become bluer with height, the normal galaxies have an approximately constant color, and the stripped galaxies are strikingly blue

near the disk and similar to the normal galaxies at larger heights. However, some variation in the color with height is seen in a few individual normal galaxies. More data are necessary to determine if this is similar to what is seen in the starbursts.

### 5.4. Correlation Analysis for Average Properties

We compared the total halo fluxes, FUV–NUV colors, and the scale heights to the following galaxy parameters: the UV luminosity of the galaxy ( $L_{\text{gal}}$ , corrected for internal extinction), the star-formation rate (SFR) and specific SFR (sSFR), the  $H\alpha$  luminosity of the galaxy ( $L_{H\alpha}$ ), the stellar mass ( $M_*$ ), the rotation velocity ( $v_{\text{rot}}$ ), the morphological type code ( $T$ ; de Vaucouleurs et al. 1991), the inclination ( $i$ ), and the distance from Earth ( $d$ ).

$L_{H\alpha}$ ,  $v_{\text{rot}}$ ,  $T$ ,  $i$ , and  $d$  come from NED and HyperLeda values. Some of the  $H\alpha$  fluxes include some flux from the neighboring [NII] line. We compute  $M_*$  from the  $K$ -band luminosity from the 2MASS Extended Source Catalog and the mass-to-light ratio from Bell & de Jong (2001), for which we use  $B-V$  colors from HyperLeda. The SFR is based on the relation from Kennicutt (1998), which uses far-infrared (FIR) fluxes measured with the IRAS satellite. Fluxes exist for all but one galaxy (NGC 4217). The values we use are reported in Table 1.

We estimated  $L_{\text{gal}}$  in each filter by “de-reddening” the measured flux following Buat et al. (1999), who found a relation for the UV extinction based on the far-infrared (FIR) and measured UV fluxes. The relation is best cal-

TABLE 6  
DIFFUSE HALOS

Name	FUV–NUV (mag)	Scale Height (kpc)	$\chi^2_\nu$	(H $\alpha$ )	Extrplanar Diffuse?			$F_{\text{FIR}}$	$A_{0.16}$ (mag)	$A_{0.2}$ (mag)	(FUV)	$L_{\text{halo}}$ ( $uvm2$ )	(FUV)	$L_{\text{gal}}$ ( $uvm2$ )	$L_{\text{halo}}/L_{\text{gal}}$ (FUV)	$L_{\text{halo}}/L_{\text{gal}}$ ( $uvm2$ )
(1)	(2)	(3)	(4)	(5)	(X-ray)	(160 $\mu\text{m}$ )	(GHz)	(9)	(10)	(11)	(12)	(13)	(14)	(15)	(16)	(17)
Starbursts																
NGC0253	1.26 $\pm$ 0.02	2.2 $\pm$ 0.1	38	Y	Y	Y	Y	67.6	3.6		6.9		1448.2		0.005	
M82	0.87 $\pm$ 0.02	2.7 $\pm$ 0.1	32	Y	Y	Y	Y	86.8	7.5	6.2	13.0	24.6	2621.6	3151.3	0.005	0.008
NGC4631	0.73 $\pm$ 0.03	1.8 $\pm$ 0.1	1.3	Y	Y	Y	Y	6.4	1.5	1.2	11.9	21.8	612.7	648.2	0.019	0.035
NGC3628	1.55 $\pm$ 0.08	3.9 $\pm$ 0.2	1.8	Y	Y	N	N	5.7	4.1	3.0	6.5	17.2	1347.4	1128.5	0.005	0.016
NGC4666	0.90 $\pm$ 0.08	7.6 $\pm$ 0.4	0.3	Y	Y	Y	Y	3.9	3.7	3.0	8.2	12.9	2333.3	1932.9	0.003	0.007
NGC3079	0.35 $\pm$ 0.01	3.4 $\pm$ 0.1	1.6	Y	Y	Y	Y	4.9	3.3	2.6	18.7	28.0	3772.2	3214.7	0.005	0.009
NGC5775	0.59 $\pm$ 0.04	4.5 $\pm$ 0.3	2.6	Y	Y	Y	Y	2.3	4.0	3.2	11.4	19.8	1887.0	1563.7	0.006	0.013
NGC4388	1.02 $\pm$ 0.06	2.7 $\pm$ 0.1	3.5	Y	Y	Y	Y	1.1	3.0	2.1	6.0	14.6	945.9	878.7	0.006	0.017
Normal Spirals																
NGC0055	2.8 $\pm$ 0.6	1.1 $\pm$ 0.1	4.2	Y	N	Y		4.0	0.5		0.5		65.7		0.007	
NGC0891	0.33 $\pm$ 0.09	1.5 $\pm$ 0.2	0.8	Y	Y	Y	Y	6.8	5.0	4.3	6.9	11.4	1088.3	1043.1	0.006	0.010
NGC2683	2.0 $\pm$ 0.4	2.7 $\pm$ 0.2	0.9	N	N		N	1.1	2.3	1.7	3.6	5.8	203.6	219.7	0.018	0.025
NGC4517	1.5 $\pm$ 0.2	3.4 $\pm$ 0.2	1.9			Y		0.7	1.9		3.1		152.2		0.020	
NGC4565		2.0 $\pm$ 0.3	0.7	N	N	N	N	1.2								
NGC4096	1.8 $\pm$ 0.3	4.3 $\pm$ 0.3	0.7	N		Y	N	0.9	2.0	1.5	1.9	7.9	277.6	312.3	0.007	0.024
NGC4313	1.0 $\pm$ 0.3	6.6 $\pm$ 3.3	2.7					0.2	3.9		1.3		73.7		0.021	
NGC3623	3 $\pm$ 3.	4 $\pm$ 1.	3	N	N		N	0.6	2.3	1.4	0.4	3.3	169.9	209.4	0.002	0.015
NGC5907	0.74 $\pm$ 0.09	6.4 $\pm$ 0.2	1.3	N	N	Y	N	1.7	2.5	2.0	7.1	13.8	816.6	829.1	0.009	0.016
NGC4216	1.6 $\pm$ 0.3	3.4 $\pm$ 0.3	0.9	N		N	N	0.3	2.6		2.7		160.1		0.017	
NGC4607	1.2 $\pm$ 0.4	3.7 $\pm$ 1.3	1.0			N		0.4	4.7		0.8		202.1		0.004	
NGC4522	0.55 $\pm$ 0.04	1.9 $\pm$ 0.1	1.8	Y		Y		0.2	1.6		6.0		139.4		0.043	
NGC0134		1.9 $\pm$ 0.3	0.7					2.8		2.5		10.1		1548.1		
NGC4157	0.8 $\pm$ 0.1	4.7 $\pm$ 0.5	2.1	N			Y	2.0	3.6		6.3		1171.6		0.005	
ESO358	1.2 $\pm$ 0.1	5.3 $\pm$ 0.9	0.1					0.5	2.8		2.6		296.9		0.009	
NGC4217	1.2 $\pm$ 0.2	3.1 $\pm$ 0.4	0.1	Y	Y	Y	Y				7.6					
NGC4330	0.51 $\pm$ 0.03	1.1 $\pm$ 0.1	1.6					0.1	1.7	1.4	5.1	6.9	101.7	116.5	0.050	0.055
NGC3044	0.2 $\pm$ 0.1	3.8 $\pm$ 0.7	0.8	Y	Y		Y	1.1	2.4	1.9	6.7	6.0	998.1	1011.2	0.007	0.006
NGC5170	3 $\pm$ 2.	7.9 $\pm$ 0.5	0.8	N	N			0.2	1.5		3.6		269.1		0.013	

REFERENCES. — The presence of extraplanar diffuse emission was determined from the literature. H $\alpha$ : Rossa & Dettmar (2003a), X-ray: Strickland et al. (2004); Tüllmann et al. (2006); Li & Wang (2013), Radio: Wiegert et al. (2015)

NOTE. — Cols. (1) Name (2) FUV–NUV color averaged over the halo (3-4) Best-fit scale height to combined data from all wavebands and reduced  $\chi^2$  (5-8) Is there extraplanar diffuse emission? (9) FIR flux used to determine galactic extinction in units of  $10^{-9}$  erg s $^{-1}$  cm $^{-2}$  (10-11) Estimated extinction in the FUV and  $uvm2$  bands from Buat et al. (1999) (12-13) Halo luminosity density in units of  $10^{25}$  erg s $^{-1}$  Hz $^{-1}$  (13-14) De-reddened galaxy luminosity density in units of  $10^{25}$  erg s $^{-1}$  Hz $^{-1}$  (15-16) Halo-to-galaxy luminosity ratio using de-reddened galaxy luminosity.

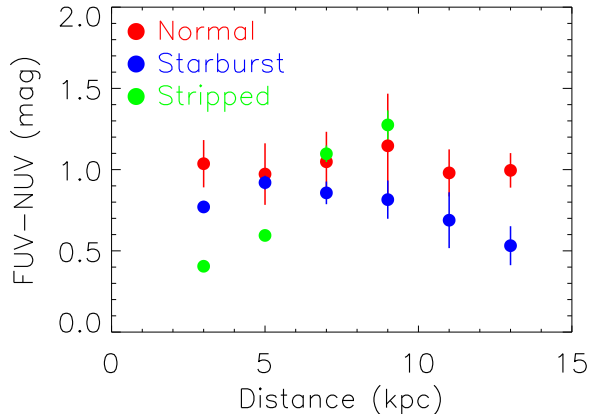


FIG. 10.— FUV–NUV color as a function of height for composites of the normal, starburst, and stripped galaxies in our sample.

ibrated for the FUV and *uvm2* filters, so we focus on these filters. We further correct  $L_{\text{gal}}$  for the light that would escape the galaxy assuming an extinction out of the disk of 0.5 mag in the *B* band (Calzetti 2001). We convert this to the extinction in the FUV and *uvm2* filters using a modified Calzetti et al. (2000) law from Kriek & Conroy (2013), who derived extinction curves for composite galaxy SEDs. Following their scheme, we adopt an attenuation slope of  $\delta = -0.2$  for the starbursts and  $\delta = 0.0$  for the normal galaxies, and a 2175Å bump strength of  $E_b = 0.5$  or 1.0 for starbursts and normal galaxies, respectively. These are both more similar to the Calzetti et al. (2000) law than the traditional Milky Way extinction law towards (Weingartner & Draine 2001). This leads to  $A_{\text{FUV}}/A_B = 2.05$  and  $A_{\text{uvm2}}/A_B = 1.96$  for the starburst galaxies, whereas  $A_{\text{FUV}}/A_B = 2.5$  and  $A_{\text{uvm2}}/A_B = 2.2$  for the normal galaxies. These parameters are appropriate for star-forming galaxies, but the analysis below is insensitive to the exact  $\delta$  or  $E_b$ , or whether  $L_{\text{gal}}$  includes attenuation along the minor axis. The measured  $L_{\text{gal}}$ , the estimated extinction, and the corrected values are given in Table 6.

We used Spearman’s rank correlation with a significance threshold of  $p = 0.05$  to search for correlations between galaxy and halo properties. A summary of the findings is given in Table 7. Here we describe the results and give the correlation coefficient ( $R$ ) and  $p$ -value for correlations with  $p < 0.05$ . As we tested for correlations between a range of measurements, we adopted the Benjamini & Hochberg (1995) procedure to control for false positives, also using a threshold of  $\alpha = 0.05$ . There were 61 total comparisons. Correlations with  $p$ -values that remain significant for the revised threshold are noted in Table 7 and discussed below.

The halo luminosity  $L_{\text{halo}}$  is strongly correlated with  $L_{\text{gal}}$ , with  $R = 0.87$  and  $p < 10^{-8}$  in FUV and  $R = 0.79$  and  $p = 8.3 \times 10^{-4}$  in *uvm2*. It is also correlated with the SFR in both ( $R = 0.82$  and  $p = 8.5 \times 10^{-7}$  for the FUV and  $R = 0.77$  with  $p = 0.0012$  in *uvm2*), and with the specific SFR ( $R = 0.64$  and  $p = 0.0016$  in FUV and  $R = 0.59$  and  $p = 0.033$  in *uvm2*).  $L_{\text{H}\alpha}$  is closely related to the SFR, but whereas there is a significant correlation between  $L_{\text{halo}}$  and  $L_{\text{H}\alpha}$  in the FUV ( $R =$

0.62,  $p = 0.0041$ ) there is no significant correlation for *uvm2* ( $p = 0.12$ ).  $L_{\text{halo}}$  is correlated with morphological type for *uvm2* ( $R = 0.58$ ,  $p = 0.030$ ) but not for the FUV ( $p = 0.12$ ). Overall, the  $p$ -values are smaller for the FUV, possibly because there are 24 FUV measurements and 15 *uvm2* measurements. There is no other significant correlation between  $L_{\text{halo}}$  and the other parameters in either filter.

$L_{\text{halo}}$  is also correlated with the FUV–NUV color for the FUV band ( $R = 0.52$ ,  $p = 0.00076$ ), but not *uvm2* ( $p = 0.11$ ). The FUV–NUV color is significantly correlated with the specific SFR ( $R = 0.48$ ,  $p = 0.028$ ) but not the SFR ( $p = 0.076$ ), nor with  $L_{\text{gal}}$  in either FUV or *uvm2* ( $p = 0.051$  and  $p = 0.38$ , respectively). There are no other significant correlations between FUV–NUV and other galaxy properties.

In addition to the FUV  $L_{\text{halo}}$ , the FUV–NUV color is correlated with the FUV  $L_{\text{gal}}$  ( $R = 0.41$ ,  $p = 0.048$ ). It is not correlated with other halo luminosities. FUV–NUV is also marginally correlated with sSFR ( $R = 0.48$ ,  $p = 0.03$ ), but the correlation with SFR is not significant. There are no other significant correlations between FUV–NUV and the galaxy properties.

We also compared  $L_{\text{halo}}/L_{\text{gal}}$  to the galaxy properties for the FUV and *uvm2* filters.  $L_{\text{halo}}/L_{\text{gal}}$  is correlated with the SFR ( $R = 0.42$  and  $p = 0.042$  for the FUV, and  $R = 0.59$  with  $p = 0.027$  for *uvm2*). There are no other significant correlations with other properties.

The scale height  $h$  is not correlated with any galaxy or halo property except  $d$ , where  $R = 0.47$  and  $p = 0.012$ . This is almost entirely due to NGC 5170 ( $h = 7.9$  kpc), which is near the distance cutoff and has an unusually large value.

Applying the Benjamini-Hochberg procedure for  $\alpha = 0.05$  and 61 tests, we find that the following correlations are significant: in both FUV and *uvm2*  $L_{\text{halo}}$  is correlated with  $L_{\text{gal}}$  and with the SFR, and  $L_{\text{halo}}$  is correlated with FUV–NUV, specific SFR, and  $L_{\text{H}\alpha}$  in the FUV only. The other correlations with  $p < 0.05$  described above are not significant at this threshold.

In summary,  $L_{\text{halo}}$  is related to  $L_{\text{gal}}$  and some the metrics of star formation, as well as the halo color. However, the scale height has no (strong) dependence on the halo or intrinsic galaxy properties.

### 5.5. Average Properties and Morphology

For most galaxies in the *GALEX* and *Swift* archive it is not possible to examine the morphology in detail because of low  $S/N$  or large distance. Thus, we compare the average properties  $L_{\text{halo}}$ , FUV–NUV, and  $h$  to the UV maps in Figures 3 and 4. Overall, we find that averaging obscures the presence of halo components such as winds, filaments, or bright emission near the disk, so that these properties are not useful metrics of the halo morphology.

Apart from the clear divide between normal and starburst galaxies,  $L_{\text{halo}}$  appears unrelated to the halo morphology, except in stripped galaxies. For example, NGC 5907 has a very patchy, low  $S/N$  halo in Figure 3, but its  $L_{\text{halo}}$  is among the highest of the normal galaxies. Since we know that  $L_{\text{halo}}$  is uncorrelated with  $h$  it does not provide information about the halo structure. Likewise, the most spectacular UV halos around starburst galaxies (M82, NGC 253, NGC 4631, and NGC 3079) have similar  $L_{\text{halo}}$ . The stripped galaxies

TABLE 7  
UV HALO CORRELATIONS

Quantity (1)	$L_{\text{halo}}$ (FUV) (2)	$L_{\text{halo}}$ ( <i>uvm2</i> ) (3)	$L_{\text{halo}}/L_{\text{gal}}$ (FUV) (4)	$L_{\text{halo}}/L_{\text{gal}}$ ( <i>uvm2</i> ) (5)	$h$ (kpc) (6)	FUV–NUV (mag) (7)
$L_{\text{gal,FUV}}$	0.87 <sup>a</sup>	-	N	-	N	0.41 <sup>a</sup>
$L_{\text{gal,uvm2}}$	-	0.79 <sup>a</sup>	-	N	N	N
$h$	N	N	N	N	-	N
$L_{\text{gal,H}\alpha}$	0.62 <sup>a</sup>	N	N	N	N	N
SFR(IR)	0.82 <sup>a</sup>	0.77 <sup>a</sup>	0.42	0.59	N	N
$M_*$	N	N	N	N	N	N
SFR(IR)/ $M_*$	0.64 <sup>a</sup>	0.59	N	N	N	0.48
$v_{\text{rot}}$	N	N	N	N	N	N
$T$	N	0.58	N	N	N	N
$i$	N	N	N	N	N	N
$d$	N	N	N	N	0.47	N

NOTE. — Correlations between halo quantities and galaxy and halo properties. For significant correlations ( $p < 0.05$ ) the Spearman ranked correlation coefficient is given. Non-significant correlations are marked by an ‘N’. A dash (‘-’) indicates no measurement. Cols. (1) Quantity (2-3) Halo luminosity (4-5) Ratio of halo luminosity to de-reddened galaxy luminosity (6) Scale height of the UV halo (7) Average FUV–NUV color in the halo. See text for more a more detailed description.

<sup>a</sup> These correlations survive the Benjamini-Hochberg test with  $\alpha = 0.05$  for 61 tests.

(NGC 134, NGC 4522, and NGC 4330) have unusually high  $L_{\text{halo}}/L_{\text{gal}}$  (5-10% instead of the typical 0.5-2%). As discussed earlier, this is largely attributable to extraplanar star formation.

We also find no connection between the halo morphology and the average FUV–NUV color, except insofar as bluer halos are more structured in our sample because they predominantly belong to starburst galaxies. Likewise, the scale height appears to be independent of radial concentration, although in starburst or stripped galaxies the scale height can change with galactocentric radius. The stripped galaxies cannot be distinguished from the rest of the sample by their average FUV–NUV color and are only barely distinguishable by scale height; it is not likely that these metrics could identify stripped galaxies in a wider sample.

### 5.6. Differences with HKB14

In HKB14 we measured fluxes without the PSF-wing correction and used these fluxes to find scale heights for several galaxies and measure correlations between some of the same quantities as above. The PSF-wing contamination is strongest near the disk, so we might expect  $h$  to increase when the spurious flux is removed, but this is not generally the case. However, the correlations that we find between  $L_{\text{halo}}$  and  $L_{\text{gal}}$ , the  $\text{H}\alpha$  luminosity, and the FIR SFR are stronger after  $L_{\text{halo}}$  is corrected for the PSF-wing contamination. For example, in the FUV the correlation between  $L_{\text{halo}} + L_{\text{PSF contam}}$  and  $L_{\text{gal}}$  is  $R = 0.41$  whereas between  $L_{\text{halo}}$  and  $L_{\text{gal}}$  it is  $R = 0.87$ . The lower fluxes also change the SEDs, but the only trend reported in HKB14 that is truly artificial is the uniform rise in the FUV–NUV color with height; we find in most galaxies no change with height.

Shinn & Seon (2015) investigated the role of PSF-wing contamination in several galaxies included in HKB14, and found that in two cases (NGC 24 and IC 5249) the UV halo that we reported appears to be entirely artificial. They used the *GALEX* images exclusively, and extrapolated the PSF wings from the PSF provided by the *GALEX* calibration team. Using the PSFs described in

Section 3, we agree with their findings for the *GALEX* images. For the considerably deeper *Swift* images, we find a faint UV halo around NGC 24 (which is not edge-on) and no UV halo above 2kpc around IC 5249. IC 5249 is seen edge-on has a very thin optical disk, so it is possible that any astrophysical UV halo exists primarily below this. Based on these results and the detections in our present sample, UV halos are ubiquitous but may not be universal (or universally detectable with current instruments).

## 6. DISCUSSION

### 6.1. The Diffuse UV Light is Probably a Reflection Nebula

Prior studies have argued that the UV halos are eRN on the basis that the light is too bright to come from shock-heated or photoionized gas (Hoopes et al. 2005), that line emission from starburst halos is polarized in a way that is consistent with dust scattering (Yoshida et al. 2011), that it can be successfully modeled by Monte Carlo radiative transfer scattering models (Seon et al. 2014; Shinn & Seon 2015), that it is too blue to originate in the stellar halo (HKB14), and that they are coincident with eDIG, winds, and other outflow tracers.

Our results further support this scenario:

1. The UV halos are truly diffuse, as determined by comparison with existing HST data, and they trace filamentary morphology seen at other wavelengths.
2. UV halos are a broadband phenomenon, with similar morphology seen from 1500-2600Å.
3.  $L_{\text{halo}}$  is strongly correlated with  $L_{\text{gal}}$  after de-reddening the galaxy flux, and it is strongly correlated with the SFR.
4. Extraplanar UV light is most visible above regions of active star formation as seen in  $\text{H}\alpha$ , X-ray, and

radio continuum data, but the presence or prominence of the UV halo does not depend on the presence of extraplanar H $\alpha$ , X-rays, or radio continuum. This rules out an emission nebula as the source.

5. Starburst galaxies have more luminous UV halos, but not higher  $L_{\text{halo}}/L_{\text{gal}}$  values or scale heights.
6. Starburst winds are visible through their smaller FUV–NUV colors, which appear to be superimposed on a thick disk similar to (although brighter than) that around normal galaxies.
7. The UV halo flux, color, and scale height are not significantly correlated with galaxy properties that are not closely connected to star formation.

The strong connection between  $L_{\text{halo}}$  and  $L_{\text{gal}}$  and the weak connection between  $L_{\text{halo}}/L_{\text{gal}}$  and the presence of outflows strongly suggests that UV halos are eRN. This also explains their broadband visibility and ubiquity, as non-ionizing UV photons can escape even if the disk is not porous. If UV halos are eRN, then they indicate that dust is widespread in the halos of spiral galaxies of all types. This implies that dust is long-lived in galaxy halos to the extent that it exists around galaxies without strong outflows and has a similar scale height as the dust around starburst galaxies. In the remainder of this section, we assume that the UV halos are eRN and examine some basic properties (however, we defer a detailed analysis of the UV halo SEDs to Paper III). We then discuss the results in the context of other work on extraplanar dust.

### 6.2. Dust Mass

We estimate the dust mass using Monte Carlo radiative transfer (MCRT) models based on the model described in Wood et al. (2001) and Whitney (2011), which incorporates the Henyey–Greenstein functions for the angular dependence of dust scattering and guarantees that each photon scatters once. These models are meant to be first-order estimates and are not as carefully constructed as other MCRT models of eRN such as in Shinn & Seon (2015) or Baes & Viaene (2016), but they are nonetheless useful.

In principle, the dust mass can be measured directly from the  $L_{\text{halo}}/L_{\text{gal}}$  ratio, since

$$L_{\text{halo},\nu} = L_{\text{gal},\nu}(1 - e^{-\tau_{\nu}\varpi_{\nu}}) \quad (1)$$

where  $\varpi_{\nu}$  is the scattering albedo and  $\tau_{\nu} = 1.086N_{\text{dust}}\sigma_{\nu}^{\text{ext}}$  is the optical depth.  $\sigma_{\nu}^{\text{ext}}$  is the extinction cross-section and  $N_{\text{dust}}$  the column. The extinction through the halo is low ( $\tau_{\nu} \ll 1$ ), so a single-scattering approximation is reasonable. As described in HKB14,  $\sigma_{\nu}^{\text{ext}}$  and  $\varpi_{\nu}$  can be determined from the shape of the SED, so the normalization is related to a characteristic column density from the disk through the halo. However, the measured flux at a given height above the disk cannot be straightforwardly interpreted as a dust column because the light source is not behind the dust. Thus, one must also adopt a geometric model for the halo dust and the disk emission, for which we use MCRT.

The MCRT model needs input distributions for the emission and the scattering/absorbing medium, as well

as the viewing angle and the scattering cross-section ( $\sigma_{\nu}^{\text{ext}} \times \varpi_{\nu}$ ).

We assume that the dust is embedded in the neutral medium and model the gas density using several components: a thin exponential disk, simple logarithmic spiral arms, and a thick exponential disk that represents the halo. Each exponential disk takes the form  $\rho(R, z) = \rho_0 e^{-R/R_0} e^{-|z|/z_0}$ , where  $R$  is the galactocentric radius in the plane and  $z$  is vertical height above the plane. We constrain  $\rho_0$ ,  $R_0$  and  $z_0$  by using high resolution H I maps, so we only model galaxies where we have such maps in hand: NGC 891, NGC 4631, NGC 5775, and NGC 5907.  $R_0$  in the halo is unconstrained, so we tie it to the value of  $R_0$  in the disk. The spiral arms are described by a polar equation  $r = ae^{b\theta}$ , where  $a$  is the normalization and  $b$  the rate of growth (the parametric equations for a Cartesian grid are  $x = r \cos \theta$  and  $y = r \sin \theta$ ). We choose  $a = 7$  and  $b = 0.28$  and compute  $x$  and  $y$  for  $\theta \in [0, 3\pi]$  with a minimum radius  $R = 3$  kpc. To add thickness, these spiral arms are convolved with a 3D Gaussian kernel with  $\sigma = 8$  pixels and an amplitude of  $0.1\rho_0$ , which is added to the underlying exponential disk. We fixed the parameters based on the extent of typical spiral arms, but for an edge-on viewing angle our results are insensitive to a wide range of  $a$ ,  $b$ , or spiral arm width. The lower panels of Figure 11 show the model for NGC 4631; we do not attempt to reproduce large-scale filaments or warps.

The light source consists of a very thin exponential disk with the same scale length as the thin gas disk and light from the midplane in the spiral arms, since we assume that UV light comes from young stars near the midplane and in the arms. Our results are not sensitive to the shape or the location of the spiral arms because we measure the halo fluxes by summing over  $R$  (described below).

Paper III will be devoted to modeling the SED and determining the dust size and composition, which will yield  $\sigma_{\nu}^{\text{ext}}$  and  $\varpi_{\nu}$ . Here we adopt a simpler approach by using the values from two dust models from Weingartner & Draine (2001): dust in the bar of the Small Magellanic Cloud (SMC), and dust in the Milky Way for sightlines where the extinction law  $R_V = 3.1$ . The choice of these models is motivated by the observation that the halo dust at larger radii appears to have an SMC-like extinction curve (Ménard et al. 2010), and that many galaxy disks have extinction curves similar to the Milky Way. As we shall see, the inferred dust masses for each model are similar.

The density and emission model is gridded on a  $201 \times 201 \times 201$  cube with a pixel scale of  $2.5$  pixels  $\text{kpc}^{-1}$ , and we model the galaxy at  $2000\text{\AA}$  only (where the corrected  $L_{\text{gal}}$  is most reliable). The viewing angle is matched to the inclination of each galaxy, and we apply the dust model by assuming that the extinction within the disk follows the Kriek & Conroy (2013) prescription with  $\delta = 0.0$  and  $E_b = 1.0$ , with a gas-to-dust ratio ( $G/D$ ) of 100, which is typical for spiral disks. Then, for a given halo  $G/D$  we simulate the light scattered into the line of sight above 2 kpc from the midplane and compare to the observations. We repeated this procedure for a grid of  $G/D \in [50, 1500]$  with spacing of 10 between  $G/D = 50$  to 100, and a spacing of 50 thereafter. The  $1\sigma$  acceptable

TABLE 8  
MCRT MODELS & 160  $\mu\text{m}$  MASSES

Name	Thick Disk		Milky Way Dust			SMC Dust			$M_{160\mu\text{m}}$ ( $10^6 M_\odot$ )
	$R_0$ (kpc)	$z_0$ (kpc)	$G/D$	$\chi^2_\nu$	$M_{\text{ext}}$ ( $10^6 M_\odot$ )	$G/D$	$\chi^2_\nu$	$M_{\text{ext}}$ ( $10^6 M_\odot$ )	
(1)	(2)	(3)	(4)	(5)	(6)	(7)	(8)	(9)	(10)
NGC 891	12	1.9	$60^{+80}_{-20}$	1.0	$6 \pm 3$	$50^{+120}_{-10}$	0.9	$7^{+2}_{-5}$	3.2
NGC 4631	8	2.3	$450^{+150}_{-50}$	4.6	$1.2^{+0.3}_{-0.1}$	$700^{+400}_{-200}$	4.1	$0.7 \pm 0.3$	0.7
NGC 5775	12	3.0	$250^{+50}_{-50}$	9.9	$4.0^{+0.6}_{-0.8}$	$400^{+100}_{-50}$	9.3	$2.3^{+0.4}_{-0.5}$	-
NGC 5907	17	3.0	$400^{+250}_{-150}$	1.1	$2.5^{+1.5}_{-0.8}$	$300^{+200}_{-150}$	1.4	$3.3^{+3.1}_{-1.3}$	6.1

NOTE. — Cols. (1) Name (2-3) Scale lengths for the thick exponential disk from matching H I profiles (4-6) Best-fit  $D/G$ , reduced  $\chi^2$ , and implied extraplanar dust mass above 2 kpc for models with Milky Way dust. The error bars are statistical from the MCRT fitting only and underestimate the true uncertainty. (7-9) Best-fit  $D/G$ , reduced  $\chi^2$ , and extraplanar dust mass for SMC dust. The fits were performed using a dust opacity and scattering albedo at 2000Å and *uvw2* data. See text for details. (10) Lower bound to dust mass above 2 kpc from 160  $\mu\text{m}$  fluxes. See text for details.

range shown in Table 8 is based on  $\Delta\chi^2$  on this grid. The best-fit halo  $G/D$  then implies a dust mass. For each simulation, we use  $10^7$  scattered photons (we found for several test cases that results do not differ when using  $10^8$  photons).

For each  $G/D$  we simulated an image and measured the halo light using long boxes parallel to the midplane that are analogous to those used to measure real UV halos. This binning smooths over differences between spiral arm models that are not well constrained by the data. We normalized the real and simulated fluxes to the projected galaxy luminosity, and found the best-fit  $G/D$  using the  $\chi^2$  statistic. The best fit is often not a good fit, but the simulated halos reasonably reproduce the observed scale heights and  $L_{\text{halo}}/L_{\text{gal}}$ .

As an example, we show the fit to NGC 4631 in Figure 11. The top panels show the outcome of the MCRT simulation. In the upper left panel, noise comparable to that in the *uvw2* image was added to show how far the simulated halo could be detected in the UVOT images (3 and 6 $\sigma$  contours are shown). The morphology of the observed halos is more complex than the symmetric, disk morphology that we obtain by construction, but since  $L_{\text{halo}}$  and the scale height  $h$  are not morphological indicators (Section 5), the MCRT models are reasonable proxies for obtaining  $M_{\text{dust}}$  (Seon et al. 2014). The top right panel shows the best-fit model compared to the measurements. The best-fit  $G/D$  values are  $G/D = 450^{+150}_{-50}$  for Milky Way dust and  $G/D = 700^{+400}_{-100}$  for SMC dust, which implies a dust mass above 2 kpc of  $M_{\text{dust}} = 1.2^{+0.3}_{-0.1} \times 10^6 M_\odot$  for Milky Way dust and  $M_{\text{dust}} = 0.7 \pm 0.3 \times 10^6 M_\odot$  for SMC dust. We emphasize that we do not know whether SMC or Milky Way dust is closer to the true halo composition, but the similarity in masses suggests that  $M_{\text{dust}}$  is insensitive to the dust model for a plausible range of models. The bottom panels of Figure 11 show the H I model compared to the data.

In Table 8 we give the best-fit  $G/D$ ,  $\chi^2$ , halo component parameters, and dust mass above  $|z| > 2$  kpc for the four galaxies we considered. We expect the best-fit  $G/D$  to be similar between filters, but with the current data this is not a useful test because the true extinction curve is not known, and changes in  $G/D$  are degenerate with changes in the incident spectrum. We caution that there

could be systematic shifts in  $G/D$  due to our choice of geometric model, the assumption that the dust is hosted by the neutral medium, the  $G/D$  adopted in the disk, and the scattering recipe in the MCRT code. Even if all of these are correct or unimportant, we expect the MCRT  $M_{\text{dust}}$  values to be lower limits to the halo dust in this region because shallower profiles are allowed by the H I data and could not be constrained by our UV measurements.

Bearing these caveats in mind, it is nonetheless worth noting that the MCRT  $M_{\text{dust}}$  masses are consistent with extrapolating the spherically symmetric Ménard et al. (2010) radial profile (measured between 20-1000 kpc) to 2-10 kpc, when we scale their average profile based on the ratio of the mass of each of the four galaxies considered here to their average galaxy. This suggests that there is a smooth density transition from the disk to the halo, at least in projection.

### 6.3. 160 $\mu\text{m}$ Dust Mass

The thermal emission from extraplanar dust provides a more straightforward measurement of  $M_{\text{dust}}$  because the flux is directly related to the column density. Here we use the 160  $\mu\text{m}$  images (as opposed to the other FIR bands) because 160  $\mu\text{m}$  is close to the peak of the FIR SED for cool dust and because there is more coverage of our sample with *Herschel*/PACS at this wavelength.

In most cases, the morphology of the 160  $\mu\text{m}$  emission does follow that of the UV in the sense that it tends to be brightest where the UV halo is also the brightest. However, the FIR emission is often not as extended vertically or radially as the UV halo (the exceptions being NGC 891 and NGC 4096). This could be a function of the much lower UV background or because most of the FIR maps are shallow snapshots obtained to measure emission from the disk, not the halo, as part of *Herschel* surveys (such as the *Herschel* Reference Survey; Boselli et al. 2010).

The dust mass can be obtained from the flux, provided one knows the temperature and grain emissivity law  $\beta$ . The number of grains is obtained from the flux and these quantities:

$$L_\nu = N_{\text{dust}} 4\pi a^2 Q_\nu(a) \pi B_\nu(T), \quad (2)$$

where  $Q_\nu(a) \approx (2\pi a\nu/c)^\beta$  is the dust emissivity and  $a$



the grain size. The mass implied is

$$M_{\text{dust}} = N_{\text{dust}} \frac{4}{3} \pi a^3 \rho_{\text{dust}}, \quad (3)$$

where  $\rho_{\text{dust}}$  is the intrinsic density of the material. We assume that  $a = 0.1 \mu\text{m}$  and that  $\rho_{\text{dust}} = 2 \text{g cm}^{-3}$ . There is actually a distribution of grain sizes that can be constrained with a dust model, which we defer to Paper III. However, we do not know the temperature or  $\beta$ .  $T$  is measured by fitting a modified blackbody to the far-infrared and sub-mm SED, but almost all of the galaxies in the sample lack the data to measure  $T$  in the halo.

For an order-of-magnitude estimate for comparison with the MCRT models, we assume that  $\beta = 1.5$  (in the literature it varies from 1-2 in nearby galaxies; e.g., Bendo et al. 2003; Casey 2012), and use the temperature of the cold dust measured in the disk for each galaxy. If the dust is embedded in neutral gas, its temperature will likely decline with height, so these  $M_{\text{dust}}$  values will be lower limits.

We measured  $160 \mu\text{m}$  fluxes above a projected height of 2 kpc for NGC 891, NGC 4631, and NGC 5907 from *Herschel* maps (NGC 5775 does not have *Herschel* data, and the angular resolution of *Spitzer*/*MIPS* is too poor to isolate halo flux). These fluxes are  $11.1 \pm 0.2 \text{Jy}$  for NGC 891,  $5.4 \pm 0.3 \text{Jy}$  for NGC 4631, and  $3.2 \pm 0.4 \text{Jy}$  for NGC 5907. For temperatures we use 23 K for NGC 891 (Hughes et al. 2014), 22 K for NGC 4631 (Meléndez et al. 2015), and 18 K for NGC 5907 (Dumke et al. 1997). Under these assumptions, the dust masses are  $M_{\text{dust}} = 3.2 \times 10^6$ ,  $0.7 \times 10^6$ , and  $6.1 \times 10^6$  for NGC 891, NGC 4631, and NGC 5907, respectively (Table 8).

These values are very sensitive to  $\beta$ ; if  $\beta = 2$ , the masses are about ten times larger. This highlights the need for deeper FIR data to constrain  $\beta$  in the *extraplanar* dust. Considering the large uncertainties, the masses are consistent with the MCRT values but do not provide useful constraints.

#### 6.4. Dust Spatial Variation

Some UV halos vary in FUV–NUV color with galactocentric radius (Figures 6 and 7) or height (Figure 10). If the UV halos are eRN, these differences arise either through changes in the dust or the incident spectrum, although both effects may be present. M82 provides a good example of the general behavior seen in starbursts, namely that the eRN is bluer in the wind region (Figure 7) and becomes bluer with height (Figure 10).

If the dust changes in composition with height (for example, if the fraction of silicate grains increases), the reflected spectrum could become bluer given a constant incident spectrum. Since the optical depth through the halo is small (as is clear from observing face-on galaxies), this is a good approximation. On the other hand, given that the nuclear starburst is obscured through the disk but (presumably) not along the minor axis, the incident spectrum into the halo may differ across the disk, leading to a projected change in the color. In this case, sightlines vertically above the starburst region would reflect a bluer incident spectrum than the rest of the disk. This behavior can be generalized to H II regions in the disk.

We cannot rule out either possibility, but in M82 the data suggest that the color change in height results from

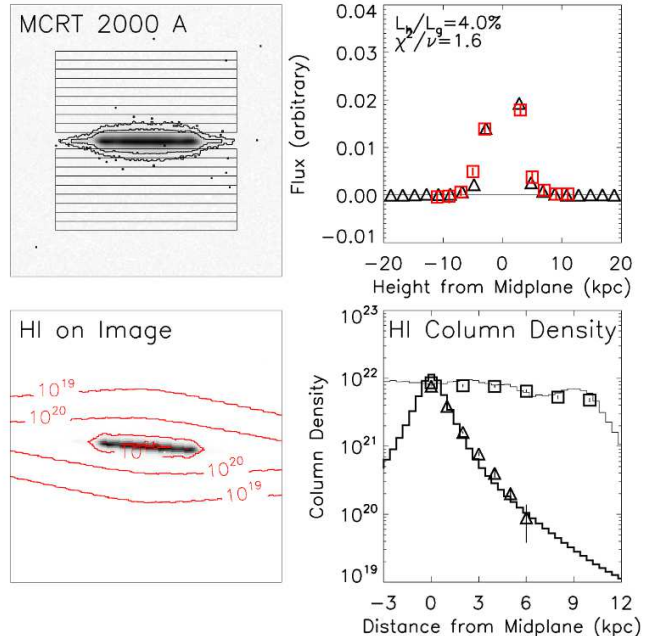


FIG. 11.— The best-fit MCRT model to NGC 4631 for Milky Way-like dust. *Top Left*: MCRT image at  $2000 \text{\AA}$  with 3 and  $6\sigma$  contours overlaid, along with flux measurement boxes. The average noise level from the *uvw2* image was added to create the contours and show the “observable” extent of the halo. *Top Right*: Measured *uvw2* fluxes from NGC 4631 compared to values measured from the MCRT model in the boxes at left. Fluxes in both cases are normalized to the measured galaxy flux. *Bottom Left*: Model H I contours overlaid on the MCRT image, which is rotated to the position angle of NGC 4631. *Bottom Right*: Measured H I column densities overlaid on our H I model. The thick black line shows the profile along the minor axis, while the thin line shows the major axis.

a change in the dust. Let us assume that the halo dust does not change. Then, for a partially obscured nuclear starburst viewed edge-on, in which light can escape along the minor axis, we expect the eRN to form bright lobes above the starburst and near the disk. These will be visible against the rest of the eRN. The lobes are bright near the disk because both the incident flux and column density are higher there. Lobes of bluer color than the rest of the eRN will also occur, with a small height offset between the bluest and brightest region. This offset occurs because the contribution to the eRN from the rest of the disk (with a redder incident spectrum) is also greatest near the disk. Above the blue lobes, the halo becomes redder as the incident flux from the starburst declines and the reflected flux from this region competes with the flux from the remainder of the disk.

We confirmed these features through MCRT models of partially obscured starbursts, as shown in Figure 12. We tried two models: a model with the same setup as described above except with 90% of the emissivity clustered in the inner 1 kpc, and a variation of this model with a “wind cone” of denser material. To examine the color we assumed that the starburst region has a Starburst 2 spectrum and the remainder of the disk has an Sc spectrum from the Kinney-Calzetti atlas (Kinney et al. 1996). We do not simulate a full spectrum, but rather determined the proper relative luminosities for the FUV and NUV bands. The cone has an opening angle of 50 degrees, a

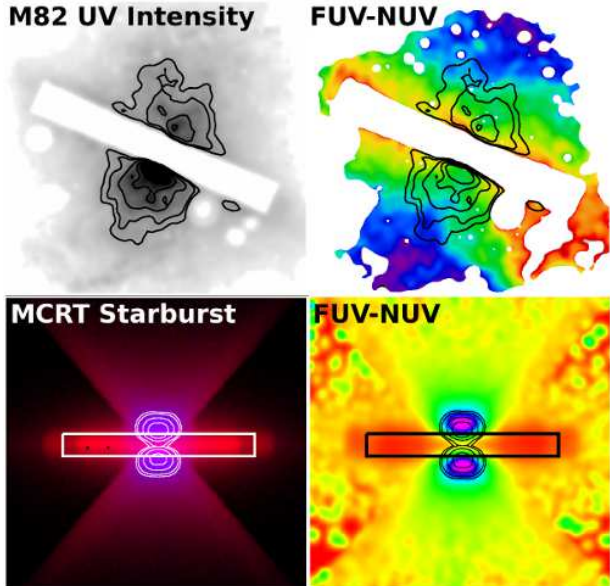


FIG. 12.— *Top Left*: Combined UV intensity map for M82. *Top Right*: FUV–NUV color map for M82. Blue or purple colors indicate where the halo is bluer, while redder colors indicate larger FUV–NUV (in magnitudes). *Bottom Left*: an MCRT simulation of an obscured starburst with a wind cone and a redder disk. The brightest region of contours from the blue light are shown. A horizontal box indicates the galaxy disk. *Bottom Right*: A synthetic FUV–NUV color map showing the halo colors with the contours from left superimposed. We expect blue “lobes”, which are not seen in M82.

width of 0.8 kpc, and a density that declines exponentially with height but is uniform at each height within the cone region. The vertical profile is  $Ae^{-b|z|}$ , where  $A$  is 1/10 of the peak, central density that is constrained by the HI data and the scale height  $b = 1$  kpc. These parameters are motivated by the appearance of limb-brightened winds in  $H\alpha$ , but are not fits to the data. We tried one additional variation in which the interior of the cone has zero density (i.e., it lacks dust).

In the case without the wind cone the main feature is the appearance of the lobes described above, whereas the remainder of the eRN looks like that for a normal disk galaxy. When the cone is present, it is brighter than the rest of the halo and its center is bluer than average, while the projected sides are relatively red. However, the presence of a cone does not change the presence of lobes in the FUV–NUV color map even if the interior of the cone is dust-free because the light is scattered by the dense cone walls.

M82 has bright lobes near the disk and there is indeed an offset between these lobes and the bluer region above, but there are no corresponding lobes in the FUV–NUV map and the color instead continues to become bluer with height and covers an increasingly large fraction of the projected area (Figure 12). These features cannot be explained by the simple geometric model above. The optical depth may be higher than we assume, which would suppress lobes in the color map, but the halo at larger heights would also be redder as the incident spectrum would change substantially through the halo. Some of the FUV light may come from line emission, but the same morphology is seen in the very deep *uvw2* image. The simplest explanation of the color map is a change in the dust with height. This could either be a physi-

cal change in a single dust component with height or an increasing contribution from one component of dust.

In other cases, such as NGC 253 or NGC 3079, there are blue regions in the halo near the bases of the winds that may indicate a different light source rather than a difference in dust (Figure 7). However, in both of these galaxies and in the composite starburst measurement, FUV–NUV color increases within a few kpc of the disk and then decreases with height (Figure 10). This suggests that these filamentary structures exist alongside an overall change in the dust with height. In contrast, most of the normal galaxies do not have significant FUV–NUV structure in Figure 6 and the composite FUV–NUV color does not appear to change with increasing height. This suggests that the dust has similar properties between 2–12 kpc. However, NGC 891 and NGC 5907 have high  $S/N$  data and show a modest decline with height above 5 kpc. Deeper data for more galaxies are necessary to determine whether the color is constant with height. Finally, in Figure 10 the stripped galaxies appear bluer than starburst galaxies at low heights and redder at larger heights. Since some of the FUV emission comes from extraplanar star formation in these few cases, we speculate that the difference is not explained by a change in the dust with height.

If the FUV–NUV color change with height around starbursts results from a change in the dust, two plausible explanations are that galactic winds eject a different type of dust and carry it to larger heights than the processes in normal galaxies, or that winds and a comparatively intense radiation field alters the pre-existing dust at large heights. In normal galaxies, the dust may circulate through a galactic fountain (Bregman 1980), which is consistent with the measured UV scale heights of several kpc. On larger scales, we expect the dust to change from Milky Way-like dust in the disk to SMC-like dust by a radius of 20 kpc (Ménard et al. 2010), which (for a given radiation field) will lead to smaller FUV–NUV color (however, cf. Smith et al. 2016, who find that most “extragalactic” dust can be explained by an extended disk). In the composite (Figure 10) we do not detect the transition through FUV–NUV color alone, but most of the galaxies do not have reliable FUV–NUV colors above 10 kpc; the values there for normal galaxies come from 2–4 galaxies, depending on the height. A clean test for this transition requires deeper data for more individual galaxies. If the dust does not change around normal galaxies up to heights difficult for a galactic fountain to reach, one possibility is that starburst episodes provide most of the halo dust.

### 6.5. M82 and NGC 891

NGC 891 and M82 both have UV halos that have been previously studied, and here we compare our maps and results to those in the literature. NGC 891 is a normal Milky Way analog with an elevated star formation rate near  $4 M_{\odot} \text{yr}^{-1}$ , (Popescu et al. 2004) and a bright X-ray halo (Bregman & Pildis 1994), whereas M82 is the archetypal superwind galaxy.

The UV halo around NGC 891 was modeled by Seon et al. (2014), who found that the UV light is consistent with a scale height between 1.2–2 kpc and a dust mass above a projected height of 2 kpc of 3–5% of the total. Hughes et al. (2014) find a dust mass in the

disk of  $M_{\text{dust}} = 8.5 \times 10^7 M_{\odot}$ , so the halo dust mass from the MCRT models in Seon et al. (2014) is between  $2.5 \times 10^6 - 4.3 \times 10^6 M_{\odot}$ . This is consistent with the MCRT scale height and mass we measured:  $h = 1.5 \pm 0.2$  kpc and  $M_{\text{dust}} = (6 \pm 3) \times 10^6 M_{\odot}$  (for Milky Way dust), whereas Seon et al. (2014) fit a profile along the projected minor axis, incorporating the core of the PSF but not the highly extended wings.

In HKB14, where we did not account for the extended PSF contamination of the halo, the UV intensity falls off more slowly with height on the side with the large H I filament, which also occurs in the X-rays and the  $160 \mu\text{m}$  image. The combined, PSF-corrected UV map shows that the part of the UV halo clearly associated with NGC 891 is brighter on that side (Figure 3), but the large-scale very diffuse emission is too extensive to be scattered light from dust around NGC 891 and may be Galactic cirrus. The increased UV intensity near the galaxy may arise from dust within the filament material adding to the total dust column.

Howk & Savage (1997) examined extraplanar dust around NGC 891 in extinction at a lower height than the UV halo, finding filamentary structures that form a thick disk and have a mass of at least a few  $\times 10^7 M_{\odot}$ , or about 10-50% of the total (Hughes et al. 2014). The resolution of their images is much higher than the UV images, so we cannot rule out the possibility that the eRN is also highly structured. However, the mass in the scattering component (estimated through MCRT or  $160 \mu\text{m}$  flux) is less than half than that inferred by Howk & Savage (1997). This is also true if we measure the diffuse dust mass between 0.5-2 kpc in our MCRT models. While they argue that it would be challenging for a galactic fountain (Bregman 1980) or radiation pressure (Ferrara et al. 1991) to lift enough dust mass to account for the extinction features they see, either mechanism could produce the smaller amount of diffuse dust inferred at large heights. This suggests that much of the dust in the chimneys falls back to the disk, and that the diffuse medium above 2 kpc is a separate component.

M82 has one of the first UV halos reported (Hoopes et al. 2005), since its extraplanar diffuse UV light is obvious from the image even without special processing. It is also the best-studied UV halo (Coker et al. 2013; Hutton et al. 2014), and the dust content of the wind has also been investigated by several authors (e.g., Engelbracht et al. 2006; Roussel et al. 2010; Yoshida et al. 2011). The consensus that the UV halo in M82 is an eRN supports the identification of other UV halos as eRN. The FIR dust emission is seen to about the same or larger distances than in the UV, implying a mass of about  $10^6 M_{\odot}$  (Roussel et al. 2010). It is more difficult to construct an accurate MCRT model for M82 than other disk galaxies because of its irregular H I morphology, but using the same method as described above we obtain a value of  $M_{\text{dust}} = 2_{-1}^{+3} \times 10^6 M_{\odot}$ , which is consistent with the FIR measurement. M82 also allows us to test our de-reddening procedure: our reported FUV  $L_{\text{gal}} = 3 \times 10^{42} \text{ erg s}^{-1}$ , whereas Coker et al. (2013) estimate that the UV luminosity seen by the halo is  $L_{\text{gal}} = 1 - 6 \times 10^{42} \text{ erg s}^{-1}$ .

We suggest that the best simple explanation for the the FUV-NUV color change with height (in M82 and star-

burst halos generally) is a change in the dust. We note that Roussel et al. (2010) show that there is little change in the  $250 \mu\text{m}/350 \mu\text{m}$  ratio in the region with the UV halo, but if the change is primarily one of composition rather than size the FIR bands may not be sensitive to it. For example, Nozawa & Fukugita (2013) successfully fit a two-component (graphite and silicate) dust model to extinction along different Milky Way and SMC sight lines by changing the mixture but fixing the size distribution using the same law found by Hutton et al. (2014). Likewise, Hutton et al. (2014) found, using shallow *Swift* data, that the dust is consistent with a single size distribution. They focused on color-color plots where a change in composition is degenerate with a change in the incident spectrum, so neither of these studies presents strong evidence against a change in the dust type with height. However, we emphasize that we have not conclusively shown that the dust composition must change.

## 7. SUMMARY AND CONCLUSIONS

We have described the morphology of UV halos around nearby, edge-on galaxies with and without superwinds, and here summarize our findings:

1. UV halos are astrophysical and can be separated from galactic light scattered into the PSF wings (Airy patterns). They are broadband phenomena and truly diffuse, with a flux of 1-20% of the apparent galaxy luminosity (a few percent or less of the de-reddened values). They are visible to beyond 10 kpc above the midplane.
2. Around normal galaxies, UV halos tend to have a thick-disk morphology, but they differ in their radial concentration and vertical prominence. In superwind galaxies, the UV halos are visible around the whole galaxy and contain filamentary structures seen at other wavelengths and associated with the winds. Galaxies that are being stripped of their ISM by ram pressure have asymmetric UV halos and some extraplanar star formation.
3. Among a variety of galactic parameters, we found that the UV halo luminosity is only correlated with the galaxy luminosity and the SFR.
4. The structure, broadband visibility, and strong correlation of  $L_{\text{halo}}$  with  $L_{\text{gal}}$  for UV halos lead us to conclude that they are eRN, which supports prior arguments made in the literature.
5. The frequency of UV halos (100% in our UV-selected sample of highly inclined galaxies within 25 Mpc) indicates that eRN are ubiquitous, but not as extensive as reported in HKB14.
6. The dust mass of the diffuse component above 2 kpc, inferred from MCRT models that are constrained by the measured  $L_{\text{halo}}/L_{\text{gal}}$  and 21-cm maps, is a few percent of the dust mass in the disk, and perhaps 10% of the dust mass seen in filamentary extraplanar structures at lower heights. Deeper FIR observations are needed to constrain  $\beta$  in the halo dust for a direct measurement.

7. There is tentative evidence for a change in the dust properties with height in starburst galaxies, but normal galaxies are consistent with constant dust properties between 2-12 kpc.

We expect virtually every star-forming galaxy to form an eRN, but their detectability in a given sample is a strong function of the UV luminosity of the galaxy and the inclination. Beyond about 25 Mpc it becomes difficult to isolate filamentary structure with *GALEX* or *Swift*, but within this limit the UV halos around normal galaxies appear smooth, and there are no clear features in the FUV–NUV color maps. One consequence is that the height profile used to constrain MCRT models (Seon et al. 2014; Shinn & Seon 2015) provides a reasonable estimate of the dust mass, assuming a thick disk morphology. UV observations of more distant starburst or wind galaxies may not discern the wind structure, but an unusually extensive or blue UV halo may indicate the presence of a wind.

Our results confirm the presence of diffuse dust around galaxies as a general phenomenon. The dust is a reliable tracer of material that, at one point, originated in a galaxy disk, so the amount and physical properties (grain size distribution, chemical composition, temperature, etc.) tell us about the role of stellar (or possibly

AGN) feedback in the history of the galaxy and the pollution of the circumgalactic medium with metals. However, much work remains: a larger, less biased sample of UV halo properties is needed, at the cost of poorer resolution. This will be addressed in Paper II. In Paper III, we will constrain dust properties in a simple model using the UV SED. Beyond this, we need to understand the dust outflow mechanism (the roles of radiation pressure and hydrodynamic entrainment), connect the UV SED to the FIR SED, and determine if (or how) the dust within 10 kpc of the galaxy connects to a larger circumgalactic component.

We thank the anonymous referee for a helpful report that improved the quality of this paper. This research has made use of the NASA/IPAC Extragalactic Database (NED) which is operated by the Jet Propulsion Laboratory, California Institute of Technology, under contract with the National Aeronautics and Space Administration. We acknowledge the usage of the HyperLeda database (<http://leda.univ-lyon1.fr>). E. H.-K. and J.C. gratefully acknowledge support from NASA grant NNH13ZDA001N-SWIFT.

*Facilities:* GALEX, Swift

#### REFERENCES

- Abramson, A., Kenney, J. D. P., Crowl, H. H., et al. 2011, *AJ*, 141, 164
- Allaert, F., Gentile, G., Baes, M., et al. 2015, *A&A*, 582, A18
- Aniano, G., Draine, B. T., Gordon, K. D., & Sandstrom, K. 2011, *PASP*, 123, 1218
- Baes, M., & Viaene, S. 2016, *A&A*, 587, A86
- Bell, E. F., & de Jong, R. S. 2001, *ApJ*, 550, 212
- Bendo, G. J., Joseph, R. D., Wells, M., et al. 2003, *AJ*, 125, 2361
- Benjamin, Y., & Hochberg, Y. 1995, *Journal of the Royal Statistical Society. Series B (Methodological)*, 57, 289
- Bertin, E., & Arnouts, S. 1996, *A&AS*, 117, 393
- Boselli, A., Eales, S., Cortese, L., et al. 2010, *PASP*, 122, 261
- Bottema, R., van der Kruit, P. C., & Freeman, K. C. 1987, *A&A*, 178, 77
- Bregman, J. N. 1980, *ApJ*, 236, 577
- Bregman, J. N., & Pildis, R. A. 1994, *ApJ*, 420, 570
- Buat, V., Donas, J., Milliard, B., & Xu, C. 1999, *A&A*, 352, 371
- Calzetti, D. 2001, *PASP*, 113, 1449
- Calzetti, D., Armus, L., Bohlin, R. C., et al. 2000, *ApJ*, 533, 682
- Casey, C. M. 2012, *MNRAS*, 425, 3094
- Chung, A., van Gorkom, J. H., Kenney, J. D. P., Crowl, H., & Vollmer, B. 2009, *AJ*, 138, 1741
- Coker, C. T., Thompson, T. A., & Martini, P. 2013, *ApJ*, 778, 79
- Collins, J. A., Rand, R. J., Duric, N., & Walterbos, R. A. M. 2000, *ApJ*, 536, 645
- Condon, J. J. 1987, *ApJS*, 65, 485
- de Vaucouleurs, G., de Vaucouleurs, A., Corwin, Jr., H. G., et al. 1991, *Third Reference Catalogue of Bright Galaxies*, ed. Roman, N. G., de Vaucouleurs, G., de Vaucouleurs, A., Corwin, H. G., Jr., Buta, R. J., Paturel, G., & Fouqué, P.
- Dumke, M., Braine, J., Krause, M., et al. 1997, *A&A*, 325, 124
- Engelbracht, C. W., Kundurthy, P., Gordon, K. D., et al. 2006, *ApJ*, 642, L127
- Ferrara, A., Bianchi, S., Dettmar, R.-J., & Giovanardi, C. 1996, *ApJ*, 467, L69
- Ferrara, A., Ferrini, F., Barsella, B., & Franco, J. 1991, *ApJ*, 381, 137
- Haynes, M. P., Giovanelli, R., & Roberts, M. S. 1979, *ApJ*, 229, 83
- Hodges-Kluck, E., & Bregman, J. N. 2014, *ApJ*, 789, 131
- Hoopes, C. G., Heckman, T. M., Strickland, D. K., et al. 2005, *ApJ*, 619, L99
- Hawk, J. C., & Savage, B. D. 1997, *AJ*, 114, 2463
- . 1999, *AJ*, 117, 2077
- Hughes, T. M., Baes, M., Fritz, J., et al. 2014, *A&A*, 565, A4
- Hutton, S., Ferreras, I., Wu, K., et al. 2014, *MNRAS*, 440, 150
- Irwin, J. A. 1994, *ApJ*, 429, 618
- Irwin, J. A., Seaquist, E. R., Taylor, A. R., & Duric, N. 1987, *ApJ*, 313, L91
- Kenney, J. D. P., & Koopmann, R. A. 1999, *AJ*, 117, 181
- Kenney, J. D. P., & Koopmann, R. A. 2001, in *Astronomical Society of the Pacific Conference Series*, Vol. 240, *Gas and Galaxy Evolution*, ed. J. E. Hibbard, M. Rupen, & J. H. van Gorkom, 577
- Kennicutt, Jr., R. C. 1998, *ApJ*, 498, 541
- Kennicutt, Jr., R. C., Lee, J. C., Funes, José G., S. J., Sakai, S., & Akiyama, S. 2008, *ApJS*, 178, 247
- Kinney, A. L., Calzetti, D., Bohlin, R. C., et al. 1996, *ApJ*, 467, 38
- Koopmann, R. A., Kenney, J. D. P., & Young, J. 2001, *ApJS*, 135, 125
- Kriek, M., & Conroy, C. 2013, *ApJ*, 775, L16
- Lee, S. W., & Irwin, J. A. 1997, in *Proceedings of the 21st Century Chinese Astronomy Conference*, ed. K. S. Cheng & K. L. Chan, 95
- Lehnert, M. D., & Heckman, T. M. 1996, *ApJ*, 462, 651
- Li, J.-T., & Wang, Q. D. 2013, *MNRAS*, 428, 2085
- Lucero, D. M., Carignan, C., Elson, E. C., et al. 2015, *MNRAS*, 450, 3935
- Makarov, D., Prugniel, P., Terekhova, N., Courtois, H., & Vauglin, I. 2014, *A&A*, 570, A13
- Martin, D. C., Fanson, J., Schiminovich, D., et al. 2005, *ApJ*, 619, L1
- McCormick, A., Veilleux, S., & Rupke, D. S. N. 2013, *ApJ*, 774, L26
- Meléndez, M., Veilleux, S., Martin, C., et al. 2015, *ApJ*, 804, 46
- Ménard, B., Scranton, R., Fukugita, M., & Richards, G. 2010, *MNRAS*, 405, 1025
- Nozawa, T., & Fukugita, M. 2013, *ApJ*, 770, 27
- Oke, J. B., & Gunn, J. E. 1983, *ApJ*, 266, 713
- Oosterloo, T., Fraternali, F., & Sancisi, R. 2007, *AJ*, 134, 1019
- Popescu, C. C., Tuffs, R. J., Kylafis, N. D., & Madore, B. F. 2004, *A&A*, 414, 45
- Rand, R. J. 1996, *ApJ*, 462, 712
- Rice, W., Lonsdale, C. J., Soifer, B. T., et al. 1988, *ApJS*, 68, 91

TABLE 9  
*Swift* MRK 501 OBSERVATIONS

<i>uvm2</i>	ObsIDs	
	<i>uvw1</i>	<i>uvw2</i>
30793006	30793001	30793006
30793007	30793002	30793007
30793008	30793003	30793008
30793009	30793004	30793009
30793010	30793006	30793010
30793011	30793007	30793011
30793012	30793008	30793012
30793013	30793009	30793013
30793014	30793010	30793014
30793015	30793011	30793015
30793016	30793012	30793016
...	...	...

NOTE. — *Swift* observations of Mrk 501 used to construct the UVOT PSF models used in this paper. The full table is available online.

TABLE 10  
*Swift* MRK 501 OBSERVATIONS

Galaxy	FUV	NUV	ObsIDs		
			<i>uvw2</i>	<i>uvm2</i>	<i>uvw1</i>
M82	G11_071001_M81	G11_071001_M81	31201001	31201001	31201001
			32503004	31201002	32503002
			32503016	32503003	32503015
			32503020	32503007	32503018
			32503028	32503008	32503022
			32503032	32503011	32503025
			32503036	32503017	32503026
			32503040	32503021	32503034
			32503046	32503024	32503043
			32503057	32503029	32503045
			...	...	...

NOTE. — *Swift* and *GALEX* observations used in this paper. The full table is available online.

- Roming, P. W. A., Kennedy, T. E., Mason, K. O., et al. 2005, *Space Sci. Rev.*, 120, 95
- Rossa, J., & Dettmar, R.-J. 2003a, *A&A*, 406, 493
- . 2003b, *A&A*, 406, 505
- Roussel, H., Wilson, C. D., Vigroux, L., et al. 2010, *A&A*, 518, L66
- Sandin, C. 2015, *A&A*, 577, A106
- Schlafly, E. F., & Finkbeiner, D. P. 2011, *ApJ*, 737, 103
- Seon, K.-i., Witt, A. N., Shinn, J.-h., & Kim, I.-j. 2014, *ApJ*, 785, L18
- Shinn, J.-H., & Seon, K.-I. 2015, *ApJ*, 815, 133
- Smith, M. W. L., Eales, S. A., De Looze, I., et al. 2016, *ArXiv e-prints*, arXiv:1607.01020
- Strickland, D. K., Heckman, T. M., Colbert, E. J. M., Hoopes, C. G., & Weaver, K. A. 2004, *ApJS*, 151, 193
- Tüllmann, R., Pietsch, W., Rossa, J., Breitschwerdt, D., & Dettmar, R.-J. 2006, *A&A*, 448, 43
- Vollmer, B., Nehlig, F., & Ibata, R. 2016, *A&A*, 586, A98
- Walter, F., Dahlem, M., & Lisenfeld, U. 2004, *ApJ*, 606, 258
- Weingartner, J. C., & Draine, B. T. 2001, *ApJ*, 548, 296
- Weliachew, L., Sancisi, R., & Guélin, M. 1978, *A&A*, 65, 37
- Westmeier, T., Koribalski, B. S., & Braun, R. 2013, *MNRAS*, 434, 3511
- Whitney, B. A. 2011, *Bulletin of the Astronomical Society of India*, 39, 101
- Wiegert, T., Irwin, J., Miskolczi, A., et al. 2015, *AJ*, 150, 81
- Wood, K., Smith, D., Whitney, B., et al. 2001, *ApJ*, 561, 299
- Yim, K., Wong, T., Xue, R., et al. 2014, *AJ*, 148, 127
- Yoshida, M., Kawabata, K., & Ohyama, Y. 2011, *PASJ*, 63, 493
- Young, J. S., Allen, L., Kenney, J. D. P., Lesser, A., & Rownd, B. 1996, *AJ*, 112, 1903
- Yun, M. S., Ho, P. T. P., & Lo, K. Y. 1994, *Nature*, 372, 530
- Zschaechner, L. K., Rand, R. J., Heald, G. H., Gentile, G., & Józsa, G. 2012, *ApJ*, 760, 37

#### APPENDIX

Tables 9 and 10 contain the *Swift* and *GALEX* observation IDs for the Mrk 501 PSF measurements and the galaxies used in this work, respectively. The *GALEX* PSF models were based on data sets for 3C 273 (obsID G14\_012003\_3C273) and PKS 2155 – 304 (obsID PKS2155m304).